Title
Investigating the Liquid State of Carbon

Author
Raj, Sumana Laxmi

Publication Date
2019

Peer reviewed|Thesis/dissertation

Investigating the Liquid State of Carbon

By

Sumana Raj

A dissertation submitted in partial satisfaction of the
requirements for the degree of
Doctor of Philosophy
in
Chemistry
in the
Graduate Division
of the
University of California, Berkeley

Committee in charge:

Professor Richard Saykally
Professor Phillip Geissler
Professor David Attwood

Fall 2019

Abstract

Investigating the Liquid State of Carbon

by

Sumana Raj

Doctor of Philosophy in Chemistry

University of California, Berkeley

Professor Richard Saykally, Chair

Carbon materials have a many contemporary applications and new carbon allotropes are being discovered. However, while graphite and diamond are well understood, very little is known about the liquid state of carbon due to the high temperatures (above 5,000 K) and pressures (above 10 MPa) required for its formation. Initial studies used electrical heating to determine the melting point of graphite and the resistivity of liquid carbon. More recent studies used non-thermal laser melting to generate a metastable liquid that was studied with visible reflectivity and X-ray spectroscopies. Shock waves have also been used to transiently generate liquid carbon. Theoretical calculations of liquid carbon initially suggested the possibility of a liquid-liquid phase transition, but later *ab initio* quantum mechanical simulations showed only a continuous change in liquid coordination as its density increased.

In this dissertation, extreme-UV (EUV) reflectivity and chirped coherent anti-Stokes Raman spectroscopy (c-CARS) were used to study non-thermally melted liquid carbon. Femtosecond laser pulses at 250 nm with a fluence of 0.45 J/cm^2 (3.5 x 10^{12} W/cm^2 intensity) were used to generate liquid carbon from an amorphous carbon substrate and the time evolution of EUV reflectivity was probed. EUV wavelengths from 20 to 42 nm were used with both *s* and *p* polarizations. The reflectivity decreased at all wavelengths probed as the material expanded and ablated. For wavelengths below 32 nm, the reflectivity decay time was less than ~2 ps. This time constant describes the lattice dynamics after melting, while above 32 nm, the reflectivity is also sensitive to the hot electron plasma generated by the melting pulse. From these results and equations for the behavior of a shock wave in a material, the electron temperature of the melted material was found to be 0.30 ± 0.6 eV. The reflectivity at two different polarizations was also used to calculate the complex refractive index of the material as it evolved over time. C-CARS spectra were obtained for highly ordered pyrolytic graphite (HOPG) and glassy carbon using CARS pump wavelengths of 400 nm and 800 nm. These spectra showed strong G peak resonance (1580 cm^{-1}), corresponding to the relative vibrations of sp^2 carbons in the material. The D peak (~1350 cm^{-1}) resonance seen in Raman scattering of disordered graphite films was not observed in the CARS spectra. As this mode occurs when the excited electron scatters from a defect or phonon, it could be that the stimulated Stokes emission that occurs during the CARS process prevents such scattering. The sample was melted with an 800 nm, 90 fs laser pulse with fluences from 0.40 to 0.85 J/cm^2 (intensities of 4.4 x 10^{12} to 9.4 x 10^{12} W/cm^2). Delay times of less than 500 fs and as long as 100 ps all showed no broadening or shifting of the G peak, as would be expected for damaging and disordering of the material; only an intensity change is seen as the material ablates. Microscope images show permanent damage to the substrate and the

fluences and times studied were comparable to those used in published reflectivity studies of liquid carbon.

To advance the study of liquid carbon, a soft X-ray second harmonic generation (SHG) technique was developed and explored. X-ray absorption provides element-specific information on the electronic structure of a material that is sensitive to the environment around the element. Combining this with the interface specificity of SHG, provides a useful technique for studying solid-solid interfaces that are difficult to study otherwise. Our first soft X-ray SHG experiments on graphite films showed that the technique was indeed highly interface specific. The technique was also sensitive to resonance amplification when the input photons were at or above the carbon K-edge. A second experiment compared the boron/vacuum interface to a buried boron/carbon (Parylene-N) interface. The technique was sensitive to interface effects, showing larger SHG intensity at the boron K-edge for the boron/Parylene-N interface compared to the boron/vacuum interface. *Ab initio* quantum simulations were used to calculate the soft X-ray SHG spectra of these systems, verifying the interface sensitivity of the technique.

Table of Contents

Acknowledgments

First and foremost, I would like to thank my advisor, Rich for his help and support over the years. I appreciate the freedom he gives his students to grow as researchers and explore different experiments. I also greatly admire his passion for science even after all these years. I would also like to thank all the members of the Saykally group. In particular Tony Rizzuto and Royce Lam provided me with invaluable guidance as I was finding my feet. Chris Hull and I worked closely throughout the years and he was a great partner for experiments and outreach activities. Will Cole and Hikaru Mizuno are both incredibly kind and hard-working researchers who I know will go on to great things. I would also like to thank Deb McCaffrey and Erika Riffe for keeping me from being the only woman in the group. I am indebted to all of our collaborators on FEL and other experiments, in particular Craig Schwartz, Walter Drisdell, Son Nguyen, Riccardo Mincigrucci, and Emiliano Prinicipi. I never expected to travel so much during graduate school, but learned a great deal from my experiments at FERMI, SACLA, and PAL. Special thanks to Ivette for keeping the Saykally group running and putting up with all of our reimbursement requests.

Friends and family have also provided a great deal of support for me through this process and kept me sane. Cal Taiji and the UC martial arts program has been a huge part of my time at UC Berkeley and I can't imagine graduate school without it. I would also like to thank Erin Creel, Ali Fischer, Iota Sigma Pi, my BASIS team, TAASTE, Elaine from TeaPress and all my other friends who gave me a place to vent about and get away from my lasers. Finally, I would like to thank my parents and sister for their constant encouragement over the years.

Chapter 1: The Liquid State of Carbon

1.1. Introduction

In addition to providing the basis for all of organic chemistry and biology, elemental carbon compounds themselves play vital roles in our world. Graphite, diamond, fullerenes, graphene, and amorphous carbon solids are used in all manner of modern applications, including electronics, batteries, manufacturing, and medical devices. However, while much is known about these solid phases of carbon, the liquid state remains very poorly understood. Due to difficulties in preparing and studying this material, its structure and properties remain essentially unknown. Characterizing the liquid state of carbon would also provide insight into other tetrahedrally coordinated liquids. Liquid water, the most common tetrahedral liquid, has many unusual properties that limit theoretical modelling of water systems [1]. Other tetrahedral liquids, such as silicon, phosphorous, and carbon are therefore relevant to expanding our understanding of water-like systems. Some theoretical studies have suggested that these liquids may exhibit liquid-liquid phase transitions [1–4], while others believe such predictions are artifacts of simulations [5,6]. Knowledge of liquid carbon could be extended to other more complex tetrahedrally coordinated liquids and help to clarify what effects are due to this specific coordination environment.

Furthermore, liquid carbon and warm dense carbon (WDC) are of astrophysical interest since carbon is the fourth most abundant element in the universe and has been proposed to comprise the cores of large planets and stars [7]. The cores of white dwarf stars, for example, are carbon-rich (~50%) and at extremely high temperatures and pressures [8]. Ice giants, such as Uranus and Neptune, contain hydrocarbons under high pressure, which could separate into pure carbon and hydrogen species [9]. Furthermore, if metallic liquid carbon does exist in the cores of planets, it would affect their magnetic properties.

Finally, unique allotropes of carbon that have interesting and useful properties can be prepared through laser melting or arc heating. While these forms are not thermodynamically stable, their high activation energies allow for use of these metastable states under a wide variety of conditions [10] In particular, carbon nanotubes have many promising commercial applications. However, the formation mechanisms are not fully understood, and therefore production of these materials is costly and inefficient. Studies have suggested that liquid carbon may be a key intermediate in these formation mechanisms [11]. These metastable solid carbon materials are discussed in more detail below.

Recent technological advances have enabled new experiments on liquid carbon and WDC samples prepared through laser melting and shock compression techniques. Additionally, a number of new, metastable states of carbon that could have unusual and promising properties have been proposed and created. In this review, we discuss the current understanding of the carbon phase diagram and describe recent experiments on liquid carbon, focusing on laser-melted carbon, as it is central to the work discussed in later chapters.

1.2. The Carbon Phase Diagram

Our current understanding of the carbon phase diagram includes at least four different solid phases, a vapor, and a liquid [10,12] (Figure 1.1). Graphite is the thermodynamically stable state of carbon at room temperature and pressure. At higher pressures, diamond becomes the thermodynamically stable state. Theoretical studies and extrapolation from experiments on silicon indicate that at even higher pressures solid carbon is found in the distorted tetrahedral BC8 state [13]. Other, even higher pressure solid phases have also been predicted by first principles' calculations [14]. Uncertainty exists in experiments and calculations of the graphite-liquid-vapor triple point, but most studies agree that it occurs at ~10 MPa and 4500 K [10,15]. The graphite-diamond-liquid triple point has been calculated to be at 15 GPa and ~4000 K and the liquid-vapor critical point has been estimated to occur near 0.2 GPa and 7000 K [10,13,16].

Initial studies of melting carbon primarily used electrical heating or thermal laser heating, and are discussed in detail in the review by Savvatimskiy et al. [15]. However, it was difficult to

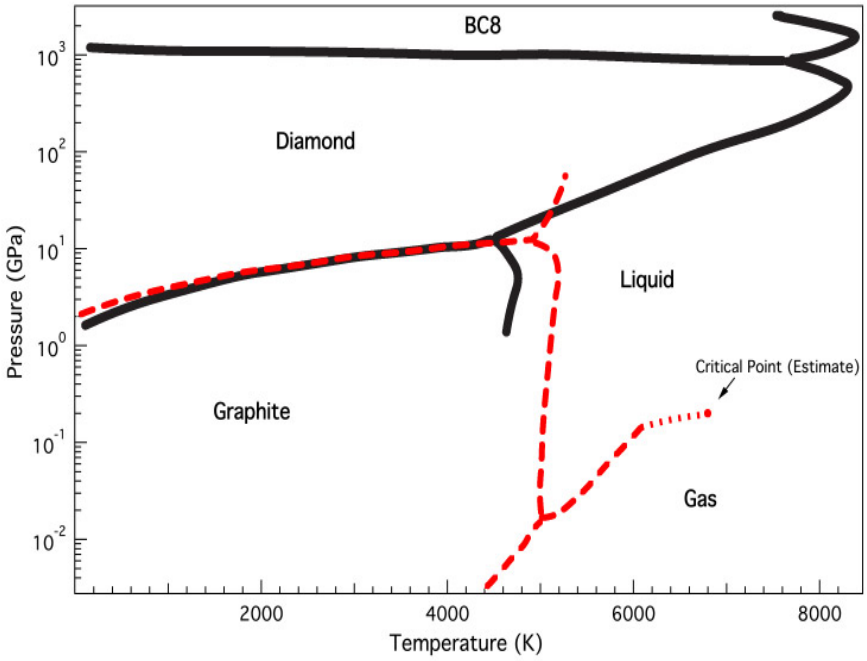

Figure 1.1: Phase Diagram of Carbon. Our current understanding of the carbon phase diagram is shown. The black solid line is taken from Zhao et al. and the red dashed line is from Bundy et al [12,10].

accurately measure the melting temperature and liquid properties due to experimental limitations on generating the high temperatures and pressures required. Slow heating, in particular, resulted in lower reported melting temperature due to complications from sublimation of the solid. The accepted values for the melting of graphite are 4800 K at pressures between 10 and 100 MPa, with a heat of fusion of 10 kJ/g [15]. Below 10 MPa, graphite sublimes and does not pass through a liquid state. These measurements also calculated the resistivity of the liquid near the melting point and a density of 1.8 g/cm^3, which is consistent for semi-metallic behavior.

Flash heating measurements of graphite melting and resistivity in the range of pressures from 1 and 10 GPa reveal a change in the slope of the graphite-liquid melting curve [10,17]. This re-entrant point was considered evidence for a graphite-liquid-liquid triple point and a phase boundary between high and low density liquids. The presence of a liquid-liquid phase transition was further supported by molecular dynamics simulations performed with an empirical Brenner potential [18]. However, later *ab initio* quantum mechanical simulations performed by the same group show a continuous change in the density of the liquid and no phase transition [19]. The classical simulations did not sufficiently account for the complex electronic interactions occurring in condensed carbon. Other simulations using first principles methods and tight-binding or semiempirical potentials also found no evidence of a liquid-liquid phase transition, and show an increase in coordination of the liquid as pressure increases [12,20–23]. Moreover, they only show metallic liquid behavior at pressures above 10^2 GPa. The diamond-BC8 phase boundary and diamond melting behavior have also been studied with *ab initio* simulations, along with supercooled liquid carbon [12,13,24]. No experiments performed thus far have been sufficiently extensive to fully explore variations in the liquid with pressure, but current experiments do not provide evidence for a liquid-liquid phase transition.

1.3. Recent Experiments on Non-thermally Melted Liquid Carbon

Ultrafast lasers, with their high peak powers and short pulse durations, have introduced new ways of preparing high energy-state materials. Among them is non-thermal melting, which is particularly advantageous, as it allows for the preparation of materials at high temperatures and pressures in a laboratory under ambient conditions. In this approach, an ultrafast laser pulse excites over 10% of the material's electron density into unoccupied states, thereby weakening its chemical bonds [25,26]. With the bonds weakened, low frequency vibrations are strong enough to disrupt and reorder the bonds, creating a transient fluid state. The liquid is formed before the material reaches thermal equilibrium, and it is inertially confined to its initial volume until the material expands and ablates. Ablation mechanisms vary depending on the melting fluence, as thermal heating and nucleation of gas, pressure waves, and fragmentation or vaporization of material can all occur [27,28]. At very high fluences—above 1 J/cm^2 (100 fs, 620 nm pulse) for silicon and gallium arsenide—sufficient material is ionized to generate a plasma [29].

Non-thermally melted silicon and gallium arsenide have been extensively through experiment—reflectivity and microscopy in particular—and theory, to explore the evolution and properties of the liquid as it forms and ablates over time [29–31]. Experiments on gallium arsenide showed disordering in 500 fs—faster than thermal heating—and a metallic liquid that persists for over 5 ps [32–35]. Under certain melting conditions, optical interference between the gas/molten liquid and liquid/solid interfaces produces a pattern of Newton rings in microscopy images of the sample. Similarly, non-thermally melted silicon is a reflective metallic liquid that persists for tens of picoseconds before ablation [36,37] [38–42].

Initial laser melting experiments on carbon used picosecond laser pulses, which are long enough in time for thermal heating, but short enough that the material can be probed before ablation begins [43]. These experiments found a melting threshold of 0.14 J/cm^2(20 ps, 532 nm pulse), which is comparable to the threshold of the non-thermal melting experiments discussed below. However, this experiment revealed a lower visible and near-IR reflectivity for the liquid than

found for solid graphite. This is in contrast to other femtosecond laser heating and electrical heating experiments on liquid carbon that show metallic behavior [44,45].

One of first studies of non-thermally melted liquid carbon were performed by Reitze et al. that measured the visible reflectivity of liquid carbon prepared by melting both diamond and highly ordered pyrolytic graphite (HOPG) with a 620 nm, 90 fs laser pulse [46]. Since the liquid is initially inertially confined to the initial density of the solid, using different solid substrates allows study of the liquid at different densities. They found that the liquid reaches a steady state with a higher reflectivity than the solid within one picosecond, and that ablation begins to distort the surface after a few picoseconds. These results are consistent with studies suggesting that liquid carbon is metallic. Following this work, Cavalleri et al. examined the reflectivity of non-thermally melted fullerenes [47]. This resulted in a lower density liquid, but its reflectivity followed the same trends as found for melted HOPG, viz. a high reflectivity steady state was reached by 1 ps, and this state persisted for over 10 ps after melting. Johnson and colleagues studied the X-ray absorption of non-thermally melted amorphous carbon samples of varying densities [48]. This study lacked the time resolution of the other experiments, and compensated for this by using a LiF coating ("tamping") to slow the expansion and ablation of the liquid. From the X-ray absorption spectra, the relative amounts of sp^2 and sp^3 carbon was determined for liquids of different densities. The results were consistent with theoretical results that predicted an increase in coordination as the density of liquid carbon increases. Visible reflectivity studies of liquid carbon are not able to elucidate the short-term (less than ~ 1 ps) evolution of the liquid, since visible light is strongly reflected by the hot electron cloud generated by the melting pulse. On the other hand, extreme UV (EUV) light is not reflected by the hot electrons and is therefore more sensitive to the underlying structure of the liquid. The EUV reflectivity of carbon decreased with melting over a time scale of ~1 ps, which indicates rapid hydrodynamic expansion and very little time wherein the material is in a well-defined thermodynamic state [49,50]. The reflectivity of liquid carbon at very short times (~100 fs) was also examined as a function of fluence and it was found that above 0.1 J/cm^2 (100 fs, 800 nm pulse), the reflectivity is constant [51]. Above this fluence, the electron-hole plasma generated by the laser pulse is sufficiently dense that energy is dissipated through charge emission and other processes that do not affect the dielectric properties of the plasma. This work also found permanent disordering of the carbon surface at fluences above 0.12 J/cm^2 (100 fs, 800 nm pulse).

High energy laser pulses can also be used to generate shock waves in a material in order to form transient high pressure states. Shock-compressed liquid carbon has been prepared by compressing graphite to 100 GPa [52]. X-ray scattering of the liquid was shown to be consistent with *ab initio* DFT-MD simulations. Shock-compressed experiments on different densities of solid carbon starting materials are also consistent with the current theoretical understanding of the phase diagram [53].

Simulations have been performed to better understand non-thermal melting dynamics of carbon. Jeschke et al. used a tight binding molecular Hamiltonian in their molecular dynamics simulations of diamond, fullerene, and graphite as they are melted with femtosecond lasers [54–56]. The electronic density of states of the liquid shows metallic character even at low densities. Formation of the liquid occurs within ~100 fs with a 50 fs melting pulse and significant ablation begins at ~1 ps. The melting threshold is very weakly dependent on both the pulse duration (for

10 to 500 fs pulses) and photon energy in the near UV and visible. Others have focused on simulating the cooling and ablation of shocked and melted carbon using density functional tight binding methods [57,58]. These simulations show the formation of carbon chains from the laser melting and subsequent cooling of graphite.

1.4. New Forms of Carbon

Liquid carbon is also of much interest as it relates to other high temperature and pressure forms of carbon and metastable forms of carbon. Warm dense carbon (WDC) is important to understanding planet and star interiors, as well as inertial confinement fusion and other explosive processes [59]. This field is growing rapidly as advances in experimental techniques and computing are making it easier to examine carbon under these extreme conditions [7,8,60]. Recent shock compression experiments have generated WDC and studied its properties and evolution with X-ray techniques [59,61]. Unique metastable carbon materials are found to form according to the initial substrate and shock parameters, and phase separation of hydrocarbons into carbon and hydrogen phases was also found to occur under these conditions [9].

There has long been interest in exotic forms of carbon generated by laser melting, and their dependence on the melting pulse duration. The redistribution of impurities after nanosecond melting of HOPG was used to establish the diffusivity of liquid carbon to be 10^{-4} cm/s^2, which is similar to other laser melted liquids [62]. The resolidified carbon from nanosecond and picosecond melting of graphite show similar characteristics based on TEM and Raman scattering measurements, indicating that time-resolved measurements are required to understand the difference between these two melting processes [63]. The study by Dallas et al. examined the crater formed by a single femtosecond laser shot and found Raman spectral features corresponding to disordered, nanocrystalline, graphite-like glassy carbon [64]. Hu et al. instead looked at the structures generated from multiple femtosecond laser shots on the same surface. Nanocrystalline diamond structures and *sp* coordinate carbon chains were both found, with the chains being most abundant at the center of the crater, where there was the highest melting fluence, and with the diamond-like material being more prevalent at the edges of the crater [65].

Studies of carbon films generated by laser ablation and deposited onto silicon substrates, show similar characteristics to the carbon structures found in the craters after melting. Comparisons of films deposited through femtosecond and nanosecond laser melting (at wavelengths of 800 nm and 308 nm, respectively), found different amounts of *sp*, sp^2, and sp^3 coordinated carbon in the films [66]. The films generated from nanosecond melting comprised 73% sp^3 diamond-like carbon, and 27% sp^2 carbon, while the films generated by femtosecond melting were 6% *sp* carbon chains, 43% sp^2, and 51% sp^3 coordinated. This difference could arise because there is less time for thermalization and reordering of the material when a shorter pulse duration is used. The same group also found that the film structure and *sp*-coordinated carbon chain content can be affected by the temperature and environment in which deposition is performed [67].

Scientists have long been fascinated about carbon allotropes and their potential applications, from the legendary discovery of fullerenes to recent work on metastable carbon states formed through laser heating. Q-carbon is one such state that has garnered much interest due to it ostensibly being harder than diamond, and ferromagnetic [68–70]. This material is made

through nanosecond laser melting of amorphous carbon and is hypothesized to be a supercooled, quenched liquid. Similarly, T-carbon (nanowires with carbon tetrahedra at each vertex of a hexagonal lattice) has recently been synthesized through picosecond laser heating of carbon nanotubes in a methanol suspension [71]. Classes of allotropes such as cyclo[n]carbons [72] (sp coordinate carbon rings), penta-graphene materials [73] (graphene like lattices of five carbon rings) and novamene [74] (combinations of sp^2 and sp^3 hexagonal carbon rings) have primarily been studied using theoretical calculations, but some forms have also been prepared experimentally. As interest in carbon allotropes grows, understanding liquid carbon will be ever more vital to understanding their formation dynamics and properties.

Understanding the nature of liquid carbon will open new fields of carbon study and will expand our knowledge of unique and useful carbon allotropes, tetrahedral liquids, and the composition of planets and stars. However, current understanding of the liquid is limited because of both the difficulties in preparing and investigating it experimentally and the complexity of calculations required to accurately capture the interactions among atoms in the liquid. Non-thermal melting, enabled by high power ultrafast lasers, and shock compression enable the preparation of liquid carbon in laboratories, allowing for studies of its reflectivity and X-ray interactions. Nevertheless, much remains to be understood about the liquid.

1.5. References

[1] M. Beye, F. Sorgenfrei, W. F. Schlotter, W. Wurth, and A. Föhlisch, Proc. Natl. Acad. Sci. (2010).
[2] Y. Katayama, T. Mizutani, W. Utsumi, O. Shimomura, M. Yamakata, and K. Funakoshi, Nature **403**, 170 (2000).
[3] O. Mishima and H. E. Stanley, Nature **396**, 329 (1998).
[4] I. Saika-Voivod, F. Sciortino, and P. H. Poole, Phys. Rev. E **63**, 011202 (2000).
[5] D. T. Limmer and D. Chandler, J. Chem. Phys. **135**, 134503 (2011).
[6] D. T. Limmer and D. Chandler, J. Chem. Phys. **138**, 214504 (2013).
[7] R. F. Smith, J. H. Eggert, R. Jeanloz, T. S. Duffy, D. G. Braun, J. R. Patterson, R. E. Rudd, J. Biener, A. E. Lazicki, A. V. Hamza, J. Wang, T. Braun, L. X. Benedict, P. M. Celliers, and G. W. Collins, Nature **511**, 330 (2014).
[8] L. M. Ghiringhelli, C. Valeriani, E. J. Meijer, and D. Frenkel, Phys. Rev. Lett. **99**, (2007).
[9] D. Kraus, J. Vorberger, A. Pak, N. J. Hartley, L. B. Fletcher, S. Frydrych, E. Galtier, E. J. Gamboa, D. O. Gericke, S. H. Glenzer, E. Granados, M. J. MacDonald, A. J. MacKinnon, E. E. McBride, I. Nam, P. Neumayer, M. Roth, A. M. Saunders, A. K. Schuster, P. Sun, T. van Driel, T. Döppner, and R. W. Falcone, Nat. Astron. 1 (2017).
[10] F. P. Bundy, W. A. Bassett, M. S. Weathers, R. J. Hemley, H. U. Mao, and A. F. Goncharov, Carbon **34**, 141 (1996).
[11] W. A. de Heer, P. Poncharal, C. Berger, J. Gezo, Z. Song, J. Bettini, and D. Ugarte, Science **307**, 907 (2005).
[12] G. Zhao, H. F. Mu, D. H. Wang, C. L. Yang, J. K. Wang, J. Y. Song, and Z. C. Shao, Phys. Scr. **88**, 045601 (2013).
[13] A. A. Correa, S. A. Bonev, and G. Galli, Proc. Natl. Acad. Sci. U. S. A. **103**, 1204 (2006).
[14] M. Martinez-Canales, C. J. Pickard, and R. J. Needs, Phys. Rev. Lett. **108**, 045704 (2012).
[15] A. I. Savvatimskiy, Carbon **43**, 1115 (2005).

[16] H. R. Leider, O. H. Krikorian, and D. A. Young, Carbon **11**, 555 (1973).
[17] M. Togaya, Phys. Rev. Lett. **79**, 2474 (1997).
[18] J. N. Glosli and F. H. Ree, Phys. Rev. Lett. **82**, 4659 (1999).
[19] C. J. Wu, J. N. Glosli, G. Galli, and F. H. Ree, Phys. Rev. Lett. **89**, (2002).
[20] C. Z. Wang, K. M. Ho, and C. T. Chan, Phys. Rev. B **47**, 14835 (1993).
[21] J. R. Morris, C. Z. Wang, and K. M. Ho, Phys. Rev. B **52**, 4138 (1995).
[22] L. M. Ghiringhelli, J. H. Los, E. J. Meijer, A. Fasolino, and D. Frenkel, Phys. Rev. Lett. **94**, 145701 (2005).
[23] L. M. Ghiringhelli and E. J. Meijer, in *Comput.-Based Model. Nov. Carbon Syst. Their Prop.* (Springer, 2010), pp. 1–36.
[24] X. Wang, S. Scandolo, and R. Car, Phys. Rev. Lett. **95**, (2005).
[25] S. K. Sundaram and E. Mazur, Nat. Mater. **1**, 217 (2002).
[26] Y Siegal, E N Glezer, L Huang, and E. Mazur, Annu. Rev. Mater. Sci. **25**, 223 (1995).
[27] D. Perez and L. J. Lewis, Phys. Rev. B **67**, (2003).
[28] K. Sokolowski-Tinten, J. Bialkowski, A. Cavalleri, D. Von der Linde, A. Oparin, J. Meyer-ter-Vehn, and S. I. Anisimov, Phys. Rev. Lett. **81**, 224 (1998).
[29] A. Cavalleri, K. Sokolowski-Tinten, J. Bialkowski, M. Schreiner, and D. von der Linde, J. Appl. Phys. **85**, 3301 (1999).
[30] N. Medvedev, H. O. Jeschke, and B. Ziaja, New J. Phys. **15**, 015016 (2013).
[31] N. Medvedev, Z. Li, and B. Ziaja, Phys. Rev. B **91**, 054113 (2015).
[32] K. Sokolowski-Tinten, J. Bialkowski, M. Boing, A. Cavalleri, and D. von der Linde, Phys. Rev. B **58**, R11805 (1998).
[33] Y. Siegal, E. N. Glezer, and E. Mazur, Phys. Rev. B **49**, 16403 (1994).
[34] P. Saeta, J.-K. Wang, Y. Siegal, N. Bloembergen, and E. Mazur, Phys. Rev. Lett. **67**, 1023 (1991).
[35] L. Huang, J. P. Callan, E. N. Glezer, and E. Mazur, Phys. Rev. Lett. **80**, 185 (1998).
[36] M. C. Downer, R. L. Fork, and C. V. Shank, JOSA B **2**, 595 (1985).
[37] C. V. Shank, R. Yen, and C. Hirlimann, Phys. Rev. Lett. **50**, 454 (1983).
[38] D. Hulin, M. Combescot, J. Bok, A. Migus, J. Y. Vinet, and A. Antonetti, Phys. Rev. Lett. **52**, 1998 (1984).
[39] A. Rousse, C. Rischel, S. Fourmaux, I. Uschmann, S. Sebban, G. Grillon, P. Balcou, E. Förster, J. P. Geindre, P. Audebert, J. C. Gauthier, and D. Hulin, Nature **410**, 65 (2001).
[40] K. Sokolowski-Tinten and D. von der Linde, Phys. Rev. B **61**, 2643 (2000).
[41] A. Rämer, O. Osmani, and B. Rethfeld, J. Appl. Phys. **116**, 053508 (2014).
[42] S. L. Johnson, P. A. Heimann, A. M. Lindenberg, H. O. Jeschke, M. E. Garcia, Z. Chang, R. W. Lee, J. J. Rehr, and R. W. Falcone, Phys. Rev. Lett. **91**, (2003).
[43] A. M. Malvezzi, N. Bloembergen, and C. Y. Huang, Phys. Rev. Lett. **57**, 146 (1986).
[44] A. M. Malvezzi and M. Romanoni, Int. J. Thermophys. **13**, 131 (1992).
[45] J. Heremans, C. H. Olk, G. L. Eesley, J. Steinbeck, and G. Dresselhaus, Phys. Rev. Lett. **60**, 452 (1988).
[46] D. H. Reitze, H. Ahn, and M. C. Downer, Phys. Rev. B **45**, 2677 (1992).
[47] A. Cavalleri, K. Sokolowski-Tinten, D. von der Linde, I. Spagnolatti, M. Bernasconi, G. Benedek, A. Podestà, and P. Milani, EPL Europhys. Lett. **57**, 281 (2002).
[48] S. L. Johnson, P. A. Heimann, A. G. MacPhee, A. M. Lindenberg, O. R. Monteiro, Z. Chang, R. W. Lee, and R. W. Falcone, Phys. Rev. Lett. **94**, (2005).

[49] R. Mincigrucci, E. Giangrisostomi, E. Principi, A. Battistoni, F. Bencivenga, R. Cucini, A. Gessini, M. Izzo, and C. Masciovecchio, Photonics **2**, 50 (2015).
[50] R. Mincigrucci, E. Principi, F. Bencivenga, L. Foglia, A. Gessini, G. Kurdi, A. Simoncig, and C. Masciovecchio, Photonics **4**, 23 (2017).
[51] A. A. Ionin, S. I. Kudryashov, S. V. Makarov, N. N. Mel'nik, P. N. Saltuganov, L. V. Seleznev, and D. V. Sinitsyn, Laser Phys. Lett. **12**, 075301 (2015).
[52] D. Kraus, J. Vorberger, D. Gericke, V. Bagnoud, A. Blažević, W. Cayzac, A. Frank, G. Gregori, A. Ortner, A. Otten, F. Roth, G. Schaumann, D. Schumacher, K. Siegenthaler, F. Wagner, K. Wünsch, and M. Roth, Phys. Rev. Lett. **111**, (2013).
[53] J. Helfrich, D. Kraus, A. Ortner, S. Frydrych, G. Schaumann, N. J. Hartley, G. Gregori, B. Kettle, D. Riley, D. C. Carroll, M. M. Notley, C. Spindloe, and M. Roth, High Energy Density Phys. **14**, 38 (2015).
[54] H. O. Jeschke, M. E. Garcia, and K. H. Bennemann, Phys. Rev. Lett. **87**, (2001).
[55] H. O. Jeschke and M. E. Garcia, Appl. Surf. Sci. **197**, 107 (2002).
[56] H. O. Jeschke, M. E. Garcia, and K. H. Bennemann, Appl. Phys. A **69**, S49 (1999).
[57] N. Goldman, S. Goverapet Srinivasan, S. Hamel, L. E. Fried, M. Gaus, and M. Elstner, J. Phys. Chem. C **117**, 7885 (2013).
[58] C. B. Cannella and N. Goldman, J. Phys. Chem. C 150722111949009 (2015).
[59] D. Kraus, J. Vorberger, J. Helfrich, D. O. Gericke, B. Bachmann, V. Bagnoud, B. Barbrel, A. Blažević, D. C. Carroll, W. Cayzac, T. Döppner, L. B. Fletcher, A. Frank, S. Frydrych, E. J. Gamboa, M. Gauthier, S. Göde, E. Granados, G. Gregori, N. J. Hartley, B. Kettle, H. J. Lee, B. Nagler, P. Neumayer, M. M. Notley, A. Ortner, A. Otten, A. Ravasio, D. Riley, F. Roth, G. Schaumann, D. Schumacher, W. Schumaker, K. Siegenthaler, C. Spindloe, F. Wagner, K. Wünsch, S. H. Glenzer, M. Roth, and R. W. Falcone, Phys. Plasmas **22**, 056307 (2015).
[60] H. D. Whitley, D. M. Sanchez, S. Hamel, A. A. Correa, and L. X. Benedict, Contrib. Plasma Phys. **55**, 390 (2015).
[61] D. Kraus, A. Ravasio, M. Gauthier, D. O. Gericke, J. Vorberger, S. Frydrych, J. Helfrich, L. B. Fletcher, G. Schaumann, B. Nagler, B. Barbrel, B. Bachmann, E. J. Gamboa, S. Göde, E. Granados, G. Gregori, H. J. Lee, P. Neumayer, W. Schumaker, T. Döppner, R. W. Falcone, S. H. Glenzer, and M. Roth, Nat. Commun. **7**, 10970 (2016).
[62] J. Steinbeck, G. Braunstein, G. Dresselhaus, M. S. Dresselhaus, T. Venkatesan, and D. C. Jacobson, J. Appl. Phys. **64**, 1802 (1988).
[63] J. Steinbeck, G. Braunstein, J. Speck, M. S. Dresselhaus, C. Y. Huang, A. M. Malvezzi, and N. Bloembergen, MRS Online Proc. Libr. Arch. **74**, (1986).
[64] T. Dallas, M. Holtz, H. Ahn, and M. C. Downer, Phys. Rev. B **49**, 796 (1994).
[65] A. Hu, M. Rybachuk, Q.-B. Lu, and W. W. Duley, Appl. Phys. Lett. **91**, 131906 (2007).
[66] A. Hu, Q.-B. Lu, W. W. Duley, and M. Rybachuk, J. Chem. Phys. **126**, 154705 (2007).
[67] A. Hu, M. Rybachuk, Q.-B. Lu, and W. W. Duley, Diam. Relat. Mater. **17**, 1643 (2008).
[68] A. Bhaumik and J. Narayan, JOM 1 (2018).
[69] J. Narayan and A. Bhaumik, J. Appl. Phys. **118**, 215303 (2015).
[70] S. Gupta, R. Sachan, A. Bhaumik, and J. Narayan, Nanotechnology **29**, 45LT02 (2018).
[71] J. Zhang, R. Wang, X. Zhu, A. Pan, C. Han, X. Li, D. Zhao, C. Ma, W. Wang, H. Su, and C. Niu, Nat. Commun. **8**, 1 (2017).
[72] K. Kaiser, L. M. Scriven, F. Schulz, P. Gawel, L. Gross, and H. L. Anderson, Science eaay1914 (2019).

[73] Z. Wang, F. Dong, B. Shen, R. J. Zhang, Y. X. Zheng, L. Y. Chen, S. Y. Wang, C. Z. Wang, K. M. Ho, Y.-J. Fan, B.-Y. Jin, and W.-S. Su, Carbon **101**, 77 (2016).
[74] L. A. Burchfield, M. A. Fahim, R. S. Wittman, F. Delodovici, and N. Manini, Heliyon **3**, e00242 (2017).

Chapter 2: Extreme-UV Reflectivity of Liquid Carbon

2.1. Introduction

Previous studies have examined the visible reflectivity of nonthermally melted liquid carbon to gain insight into the lifetime of the liquid and its resistivity [1,2]. However, those studies were not able to resolve the short-time dynamics of the lattice because the hot electron plasma generated by the melting pulse is highly reflective and masks lattice motions. Extreme ultraviolet (EUV) light is not reflected by the electron plasma and therefore can be used to characterize the lattice dynamics as the liquid is generated and evolves over time. Initial EUV reflectivity experiments showed a decrease in reflectivity over the first two picoseconds as the material disorders [3].

Subsequent experiments by Mincigrucci et al. examined the change in the EUV reflectivity of non-thermally melted liquid carbon for 19 nm to 31 nm wavelength light [4]. For all wavelengths in that range, the reflectivity decreased over time after melting with a time constant of ~1 ps. From the time constant dependence on probe wavelength, the shock-induced

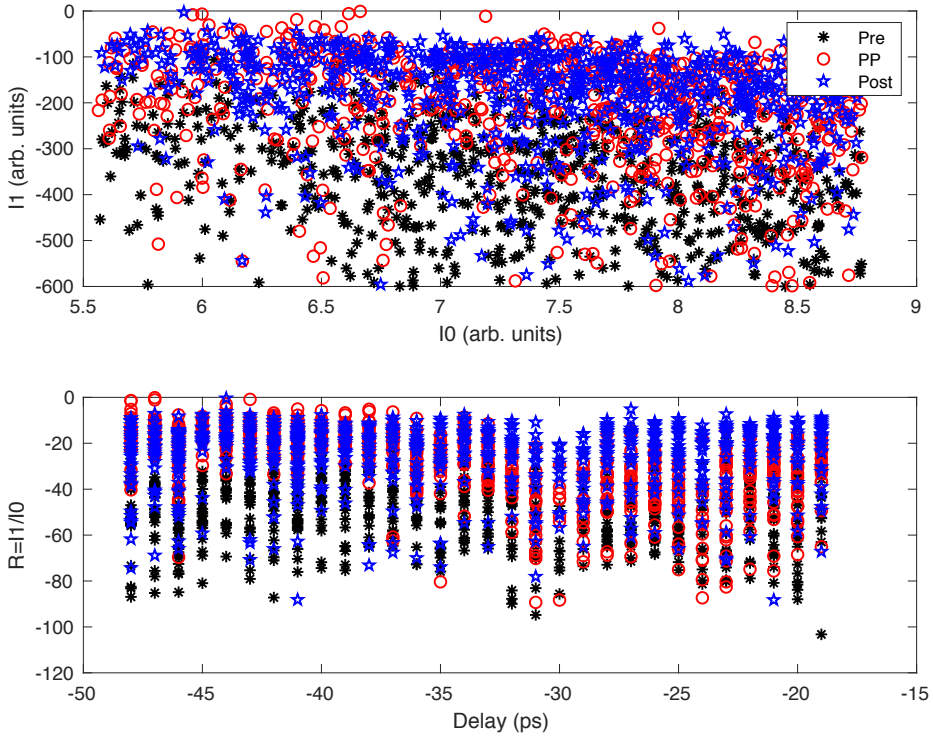

Figure 2.1: Reflectivity of amorphous carbon for each FEL shot. The top plot shows the reflected intensity (I1) as a function of the input intensity (I0) and the bottom plot shows the reflectivity (I1/I0) as a function of time delay. The data shown are for a scan taken with a FEL probe wavelength of 41.8 nm (29.7 eV), and *p* polarization. Pre-shot (*, black), on-shot (o, red), and post-shot (star, blue) results are shown. The time delay is relative to an arbitrary zero time.

expanding surface velocity (17 nm/ps) and the electronic temperature (0.8 eV) were calculated using a density gradient to describe the solid. A density-dependent two-temperature model was used to calculate electron dynamics, confirming that the EUV reflectivity is indeed insensitive to the hot electron plasma. Here we describe new efforts to expand and elaborate on these EUV reflectivity studies by extending the probe wavelength range, and using different probe polarizations and melting fluences.

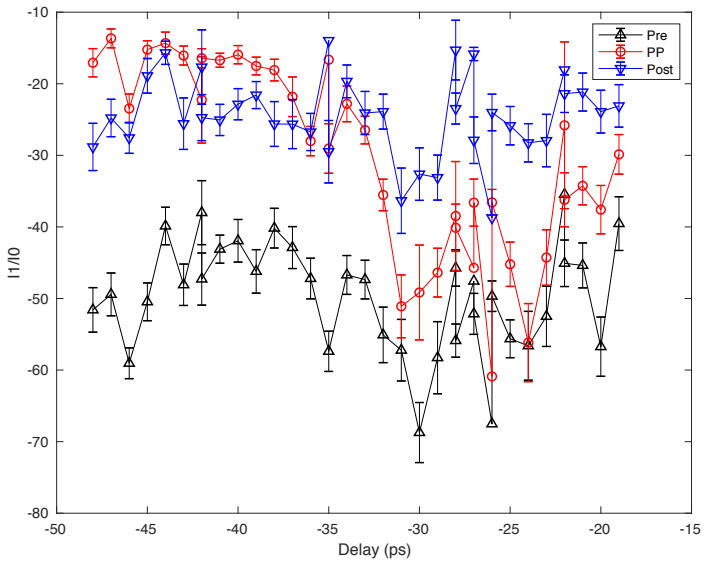

Figure 2.2: Binned reflectivity data. The binned reflectivity data are shown as a function of time delay for a probe wavelength of 41.8 nm (29.7 eV), and *p* polarization. Data are shown for the pre-shot (Δ, black), on-shot (o, red), and post-shot (∇, blue). The time delay is relative to an arbitrary zero time.

2.2. Experimental Details

We carried out these experiments at the TIMEX endstation at the FERMI free electron laser (FEL). The target, 100 nm amorphous carbon film (2.1 g/cm^3),was melted using a 251 nm, 130 fs pulse with a pulse energy of 35 μJ unless otherwise stated. With a melting spot size of 100 μm on the sample, this corresponds to a fluence of ~0.45 J/cm^2 (3.5 x 10^{12} W/cm^2 intensity), well over the non-thermal melting threshold of graphite [1,5]. Harmonics of the first stage of the FEL were used to generate ~70 fs EUV pulses at wavelengths from 21 to 42 nm (29.5 eV to 59 eV). Initially, reflectivity measurements were taken with a linear vertical (LV) FEL polarization (*s* polarized), and later experiments were performed using a linear horizontal (LH) (*p* polarized) polarization. At each time delay, reflectivity data were taken before the melting pulse (pre-shot), at the given time delay (on-shot), and then many seconds after the melting pulse (post-shot). Care was taken to ensure that the sample was not damaged by the pre-shots, and the sample was rastered after the post-shot data were acquired. Thus, the melting pulse is always incident on a pristine surface.

Figure 2.1 shows the raw data collected for a 42 nm, *p*-polarized reflectivity probe. The data were then combined into 0.5 ps bins (Fig. 2.2). The percent change in reflectivity relative to the pre-shot, unmelted solid is then fit with an exponential decay (Fig. 2.3). Zero time delay was calculated as the time after which the change in reflectivity is greater than 25%. The final reflectivity of the material at infinite time is calculated from a fit of the post-shot data to a horizontal line.

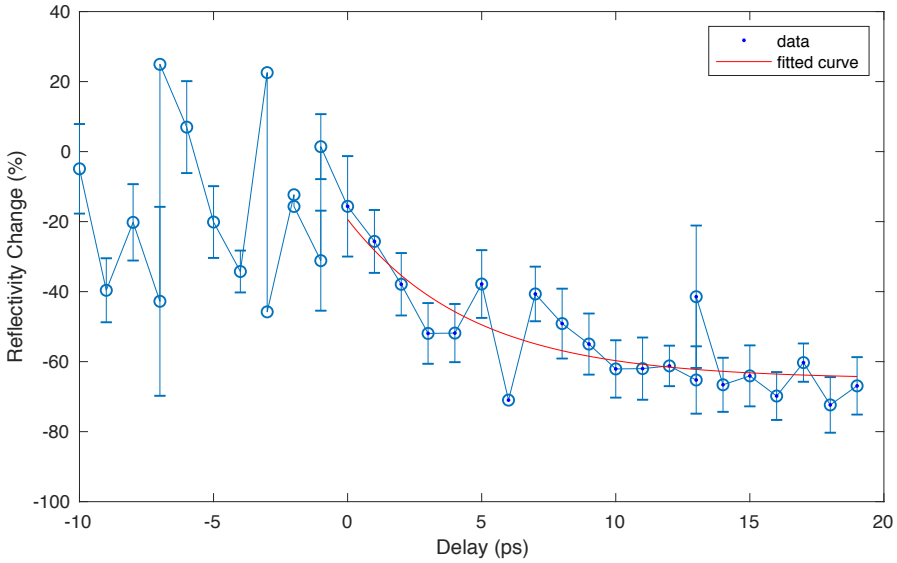

Figure 2.3: Reflectivity change vs. delay time. The percent change in reflectivity relative to the unmelted sample is shown as a function of delay time for a probe wavelength of 41.8 nm (29.7 eV), and *p* polarization. Zero-time delay corresponds to complete overlap between the melting pulse and FEL probe. The data have been fit with an exponential decay (red line).

2.3. Results and Discussion

The time constants for the different wavelengths and polarizations are shown in Figure 2.4. The time constant is weakly dependent on wavelength for the *s*-polarized data, but there is no apparent dependence for the *p*-polarized data. This is likely due to the larger errors in the *p*-polarized data due to FEL instability. The *s*-polarized data from 21 to 32 nm were fit to a line and used to calculate the expanding surface velocity and electronic temperature, as described in Mincigrucci et. al [4]. The reflectivity decay times are related to the time required for the density gradient to be comparable in length to the probe wavelength, and so the expanding surface velocity can be determined from the experimental time constants. The equation describing a shock wave in the material can then be used to extract the electronic temperature of the material from the surface velocity. The calculated expanding surface velocity is 11 ± 1 nm/ps, and the electronic temperature is 0.30 ± 0.06 eV. These values are lower than those calculated with a density-dependent two-temperature model, and consistent with work

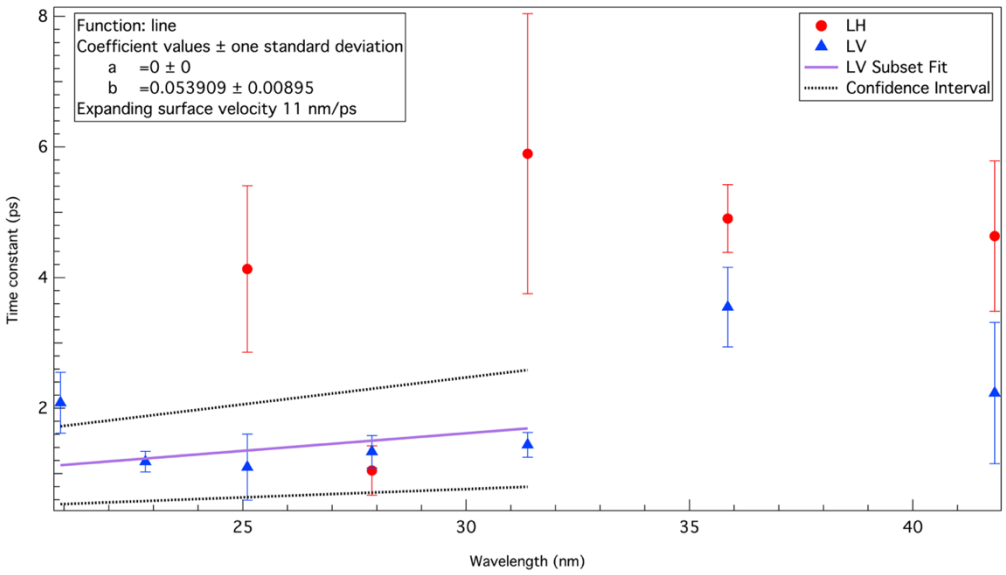

Figure 2.4: Reflectivity decay time constant as a function of probe wavelength. Decay time constants are shown for *p*-polarized (LH) (•, red), and *s*-polarized (LV) (Δ, blue) polarizations. The *s*-polarized data from 21 nm to 32 nm are fit with a line (purple) which is used to calculate the expanding surface velocity.

suggesting that a two-temperature model does not accurately capture the rapid optical phonon coupling that occurs in graphite [6].

The data from probe wavelengths above 32 nm was excluded from the fit because at those lower energies, the hot electron plasma contributes significantly to the total reflectivity. Previous work calculated the peak electron density induced by the melting pulse to be 1.6 x 10^{22} cm^{-3}, which corresponds to a plasma frequency of 5.6 x 10^{15} Hz [4]. The EUV reflectivity for this plasma frequency is shown in Figure 2.5. At wavelengths above 35 nm, the plasma reflectivity is above 20%, hence the reflectivity is no longer probes solely the lattice dynamics.

As the carbon is melted, the time evolution of the refractive index can provide insight into the liquid properties. Calculations of the complex index of refraction, ñ = n + ik, were performed for

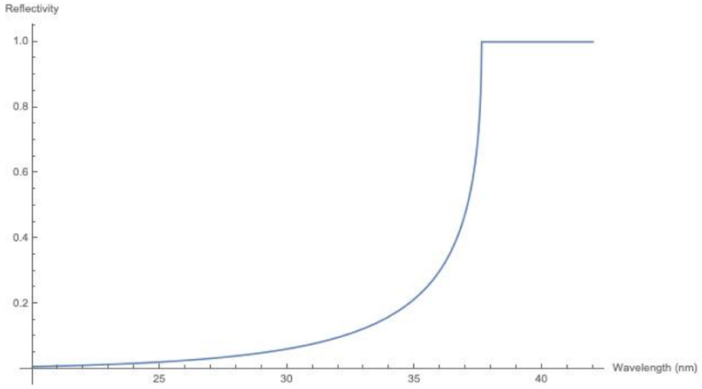

Figure 2.5: Plasma reflectivity vs. wavelength. The peak induced electron density of 1.6 x 10^{22} cm^{-3} [4], corresponds to a plasma frequency of 5.6 x 10^{15} Hz. With this plasma frequency, we can calculate the EUV reflectivity of the hot electron plasma. Above 37.6 nm (33 eV), light is completely reflected by the plasma.

wavelengths of 28 and 36 nm (Fig. 2.6). Using the Fresnel formula and the initial indices of refraction of the initial amorphous carbon solid, the index of refraction was calculated from the *s*- and *p*-polarized reflectivities at each time delay. The calculated value at 36 nm shows no apparent trend, likely due to increased error in those reflectivity data and contributions from the plasma reflectivity. However, the data taken at 28 nm show the index of refraction at long times to be 1.03+0.09i.

Data were also taken at melting pulse energies of 13-15 μJ and 26 μJ (fluences of 0.18 J/cm^2 and 0.33 J/cm^2 respectively; intensities of 1.4 x 10^{12} and 2.5 x 10^{12} W/cm^2) to examine the effects of melting fluence on EUV reflectivity. However, these data sets were very inconsistent, with a wide range of reflectivity decay constants. These inconsistencies were in part due to fluctuations in the spatial overlap of the pulses. Further studies are needed to quantify fluence effects on the EUV reflectivity.

We examined the EUV reflectivity of non-thermally melted amorphous carbon. The reflectivity was studied over time for wavelengths from 21 to 42 nm and both *s* and *p* polarizations. The s-polarized data yield a reflectivity decay constant of less than 2 ps for wavelengths below 35 nm. At wavelengths above 35 nm, the time constant increases significantly, which is in part due to contributions to the reflectivity from the hot electron plasma. The short wavelength data can be used to extract the velocity of lattice expansion and evolution. The electronic temperature calculated from the reflectivity is inconsistent with a two-temperature model, suggesting that a more complex model is required to explain the lattice dynamics. The evolution of the refractive index over time was also calculated from the 28 nm reflectivity data. Future studies should examine the effects of melting pulse fluence on the evolution of the material.

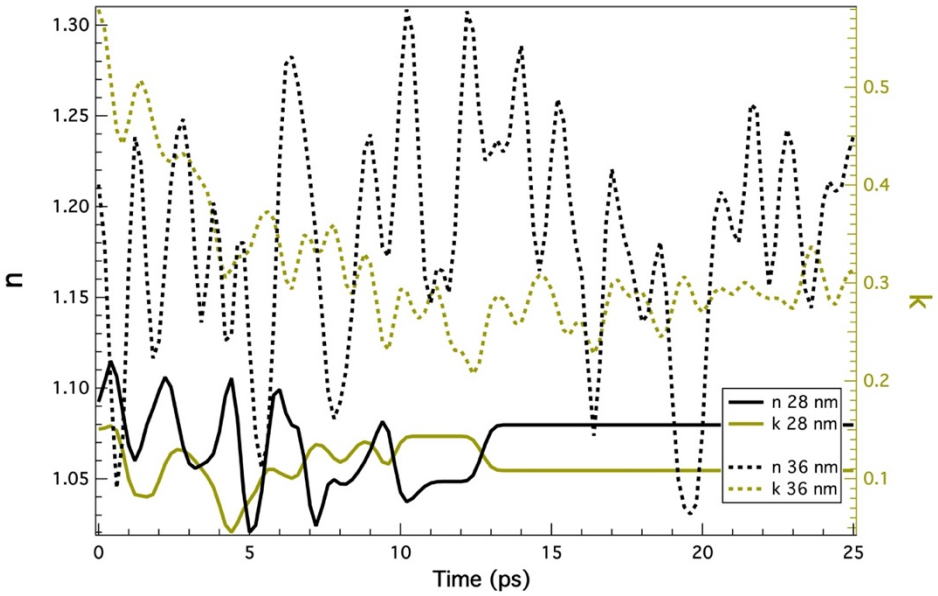

Figure 2.6: Calculated index of refraction for 28 nm and 36 nm probe wavelengths as a function of time after melting. The real (n, black) and imaginary (k, gold) components of the refractive index are shown for probe wavelengths of 28 nm (44 eV, solid) and 36 nm (24 eV, dashed).

2.4. References

[1] D. H. Reitze, H. Ahn, and M. C. Downer, Phys. Rev. B **45**, 2677 (1992).
[2] A. Cavalleri, K. Sokolowski-Tinten, D. von der Linde, I. Spagnolatti, M. Bernasconi, G. Benedek, A. Podestà, and P. Milani, EPL Europhys. Lett. **57**, 281 (2002).
[3] R. Mincigrucci, E. Giangrisostomi, E. Principi, A. Battistoni, F. Bencivenga, R. Cucini, A. Gessini, M. Izzo, and C. Masciovecchio, Photonics **2**, 50 (2015).
[4] R. Mincigrucci, E. Principi, F. Bencivenga, L. Foglia, A. Gessini, G. Kurdi, A. Simoncig, and C. Masciovecchio, Photonics **4**, 23 (2017).
[5] H. O. Jeschke and M. E. Garcia, Appl. Surf. Sci. **197**, 107 (2002).
[6] Y. Ishida, T. Togashi, K. Yamamoto, M. Tanaka, T. Taniuchi, T. Kiss, M. Nakajima, T. Suemoto, and S. Shin, Sci. Rep. **1**, 64 (2011).

Chapter 3: Coherent Anti-Stokes Raman Scattering

3.1. Background

Coherent anti-Stokes Raman Spectroscopy (CARS), is a third order nonlinear spectroscopy that is primarily used to study vibrational modes. In this parametric process, three photons interact in the material and a photon at the anti-Stokes wavelength is emitted (Fig. 3.1a). The pump pulse excites the material, and the Stokes pulse stimulates Stokes emission, leaving the material in an excited vibrational state. The probe pulse then excites the material and the anti-Stokes signal is spontaneously emitted at a frequency equal to $\omega_{pump} + \omega_{probe} - \omega_{Stokes}$. This results in a coherent, directional output, unlike the scattered signal from spontaneous Raman spectroscopy. Additionally, CARS cross-sections tend to be larger than those for Raman scattering [1]. The anti-Stokes output is at a higher photon energy than any of the input pulses and is also well-isolated from sample fluorescence. The CARS signal is generated only at the overlap of the pump, Stokes, and probe pulses, facilitating fine control of the probe depth within a sample [2].

The induced polarization of a material in response to an external electric field, can be described under the dipole approximation as

$$P \propto \chi^{(1)} E + \chi^{(2)} E^2 + \chi^{(3)} E^3 + \dots \qquad (1.1)$$

where E is the input electric field, and χ is the susceptibility of the material, which involves the overlap of the initial and final states of the material. CARS is a third-order process and the intensity is given by

$$I_{CARS} \propto |\chi^{(3)}|^2 I_{pump} I_{probe} I_{Stokes} \qquad (1.2)$$

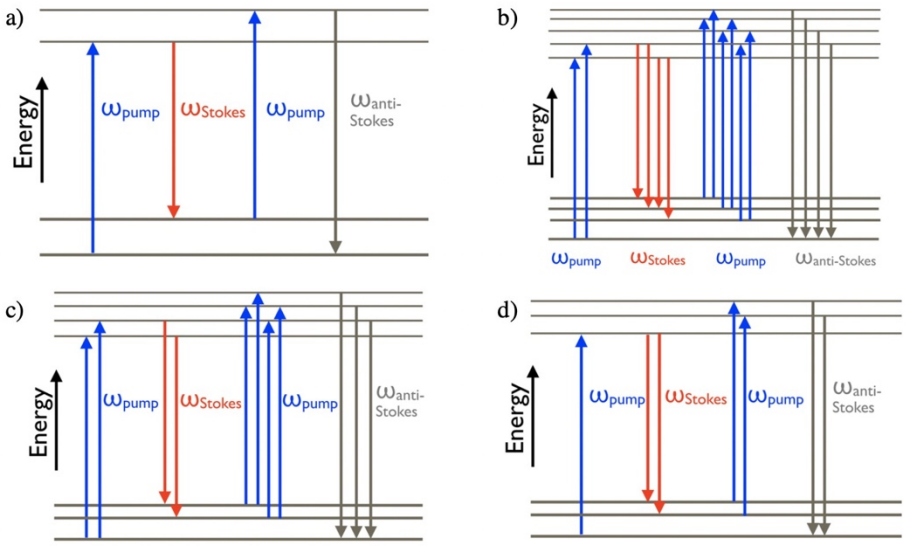

Figure 3.1: CARS energy level diagrams for picosecond pump and Stokes pulses (a), femtosecond pump and Stokes pulses (b), femtosecond pump and picosecond Stokes pulses (c), and picosecond pump and femtosecond Stokes pulses (d).

When the input and output wavelengths are resonant with real transitions in the material, $\chi^{(3)}$ becomes very large due to resonance enhancement of the signal.

CARS experiments are often performed using picosecond laser pulses. The narrow bandwidth of these pulses results in high resolution CARS spectra, but only a small range of Raman shifts is probed with a single laser shot (Fig. 3.1a). With femtosecond pulses, a larger range of Raman shifts is probed by the broader bandwidth of the pulses, but at very low resolution (Fig. 3.1b). If a broadband, degenerate CARS pump/probe and a narrowband Stokes pulse is used, the resulting spectrum is still low resolution (Fig. 3.1c). However, if a broadband Stokes pulse is combined with a narrowband pump, the resulting spectrum has high resolution and covers a wide range of Raman shifts (Fig. 3.1d). Instead of using a transform-limited picosecond pulse for the pump, a femtosecond pulse can be chirped to picosecond duration and used as the pump. Although still a broadband pulse, only a fraction of the pulse overlaps with the femtosecond Stokes pulse, and so the effective pump bandwidth is still narrow [3]. The effective resolution of the CARS spectrum, $\Delta\omega_{Spec}$, is given by

$$\Delta\omega_{Spec} = \Delta t_{Stokes} \frac{\Delta\omega_{pump}}{\Delta t_{pump}} \qquad (1.3)$$

where Δt_{Stokes} and Δt_{pump} are the FWHM pulse durations of the Stokes and pump pulses respectively, and $\Delta\omega_{pump}$ is the FWHM bandwidth of the pump pulse. A grating pair can be used to easily chirp a femtosecond pulse and the distance between the gratings can be adjusted to control the chirped pulse duration.

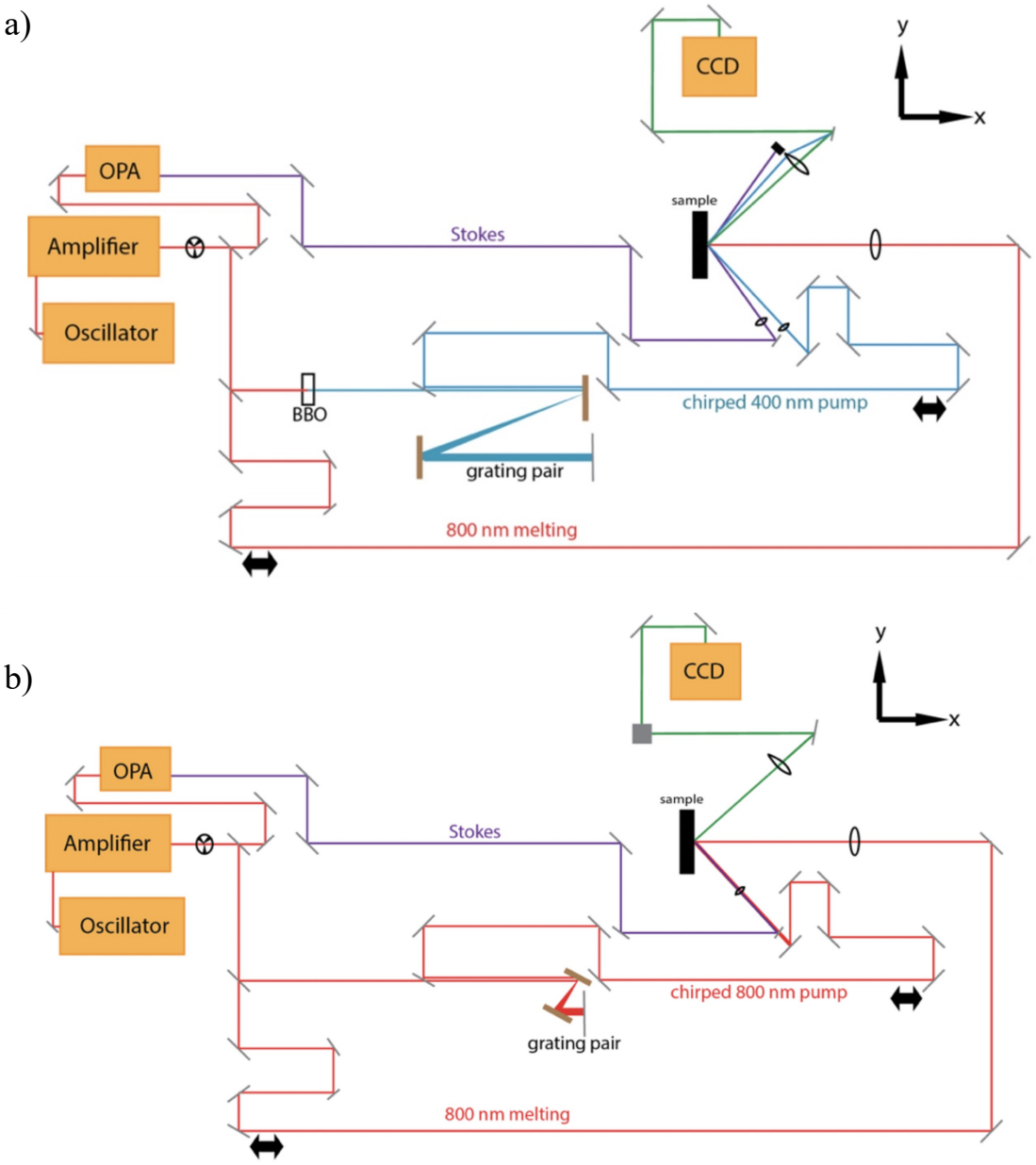

Figure 3.2: Experiment diagrams. Experimental diagrams are shown for a 400 nm CARS pump (a), and an 800 nm CARS pump (b). Double-headed arrows indicate delay stages.

3.2. Experimental Setup

The CARS system was designed using 800 nm, 90 fs laser pulses that were generated by a Spectra Physics Spitfire Ace amplifier. The output was split into three beams (Fig. 3.2a). A 2 W beam was used to pump the Light Conversion TOPAS Prime optical parametric amplifier (OPA). The OPA was used to tune the wavelength of the femtosecond Stokes pulse, in order to probe different Raman shifts, and the bandwidth of the Stokes pulse (300 cm^{-1}) is how much of the Raman spectrum is probed in a single laser shot. Stokes wavelengths from 410 nm to 450 nm

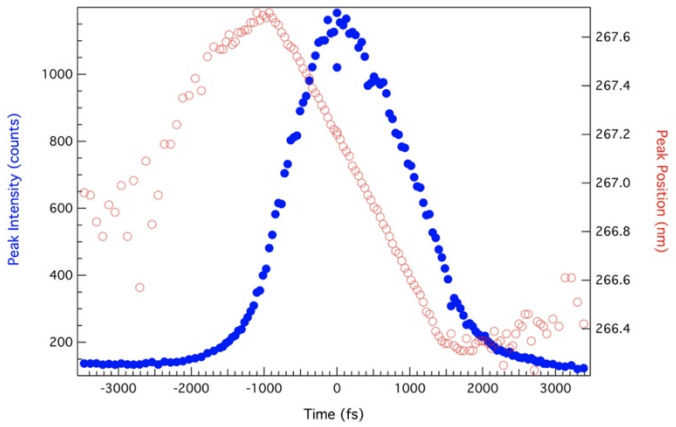

Figure 3.3: Cross-correlation of the 400 nm chirped pump pulse with a 90 fs, 800 nm pulse in a GaAs sample, where negative times indicate that the chirped pulse is incident on the sample before the femtosecond pulse. The pump pulse has a 1.86 ps FWHM duration and a chirp rate of 0.080 cm-1/fs. The pulse is negatively chirped, such that higher energy photons are incident on the sample at earlier times than lower energy photons.

were used. This experiment used a degenerate CARS pump and probe. After the amplifier, the CARS pump beam was frequency doubled to 400 nm using a BBO and then negatively chirped using a grating pair (Richardson Grating 53067BK01-330R, 400 nm blaze wavelength, 1200 grooves/mm). With a 30 cm distance between the gratings, the pulse was chirped to 1.86 ps (Fig. 3.3) resulting in a resolution of 14 cm^{-1}. A half-wave plate was used to adjust the polarization of this pulse. Taking into consideration phase matching for CARS (discussed below), the CARS pump and Stokes pulses were incident on the sample at 48°and 56°relative to the surface normal respectively. The CARS output pulse exited the sample at 40°.

An alternate setup used an 800 nm CARS pump and 840 nm to 1050 nm output from the OPA (Fig. 3.2b). The grating pair used here (Richardson Grating 53067BK01-035R, 0.9 μm blaze wavelength, 830 groves/mm) had a lower groove density, and allowed for a longer, positively chirped pulse with a duration of 10.6 ps and a spectral resolution of 2.5 cm^{-1} for the same 30 cm distance between the gratings. With these wavelengths, the CARS input and output pulses were colinear and at a 48°angle relative to the surface normal. Dichroic mirrors before and after the sample were used to combine the input pulse and isolate the CARS signal respectively.

The final laser pulse used in this experiment was the 800 nm melting pulse that was perpendicular to the sample surface. A neutral density filter wheel was used to adjust the melting pulse power. The CARS pump and Stokes pulses were focused to 50 μm diameter spots at the sample using 150 mm and 100 mm focal length lenses, respectively, while the melting pulse was focused to 150 μm using a 300 mm focal length lens on a linear micrometer stage. These spot sizes were chosen to ensure that the CARS pulses would only probe melted area. The CARS pump and Stokes pulse energies were 1 μJ each at the sample to ensure that no sample damage occurred due to these pulses. The CARS signal was detected using an Acton 300i spectrograph and Princeton Instruments PIXIS 2KBUV CCD camera. A 370 nm, 36 nm FWHM bandpass filter (Semrock) was inserted before the CCD to reduce any background from the CARS pump and Stokes pulses.

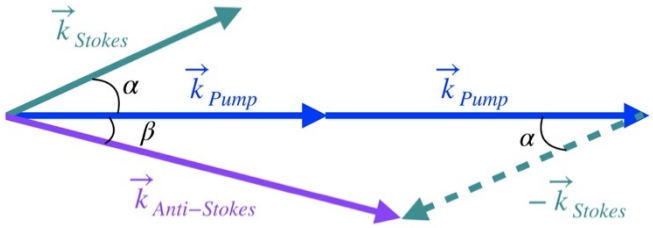

Figure 3.4: Phase matching condition for CARS where $\vec{k}_{Anti-Stokes} = 2\,\vec{k}_{Pump} - \vec{k}_{Stokes}$. Here, $\vec{k}_i = n_i\omega_i$, where n_i is the index of refraction of the material at the frequency specified by ω_i. α is the angle between the pump and Stokes rays and β is the angle between the pump and anti-Stokes rays.

As the sample was damaged by the melting pulse, the sample needed to be moved in between laser pulses so that a pristine surface is probed with each laser shot. To this end, the sample was mounted on an Opto-Sigma motorized translation stage (SGSP33-50x, SGSP33-50z), that translated the sample in the horizontal and vertical in a series of s-curves. The position of the sample along the surface normal was adjusted with a manual micrometer stage. A LabVIEW program was written to control the sample rastering and CCD camera. The sample stage movement speed was limited to 80 mm/s in x and 30 mm/s in z, which was not fast enough to refresh the sample given the amplifier repetition rate of 1 kHz and the 150 μm melting spot diameter. Therefore, a chopper was inserted immediately after the amplifier in order to decrease the repetition rate to 0.5 kHz. The CCD collected data throughout the rastering process in a single exposure. Changes of movement direction and movement in z were slow, such that overlap of laser shots occurred. These motions were performed off the sample surface and so contributed a negligible amount to the total signal.

In order for momentum and energy to be conserved, the phase matching conditions for CARS must be satisfied. From the ray diagram in Figure 3.4, the phase matching condition is given in equation 3.4.

$$\cos(\beta) = \frac{2n_{Pump}\omega_{Pump} - n_{Stokes}\omega_{Stokes}\cos(\alpha)}{n_{Anti-Stokes}\omega_{Anti-Stokes}} \quad (3.4)$$

The CARS signal is maximized when the input pulses all have the same polarization. While

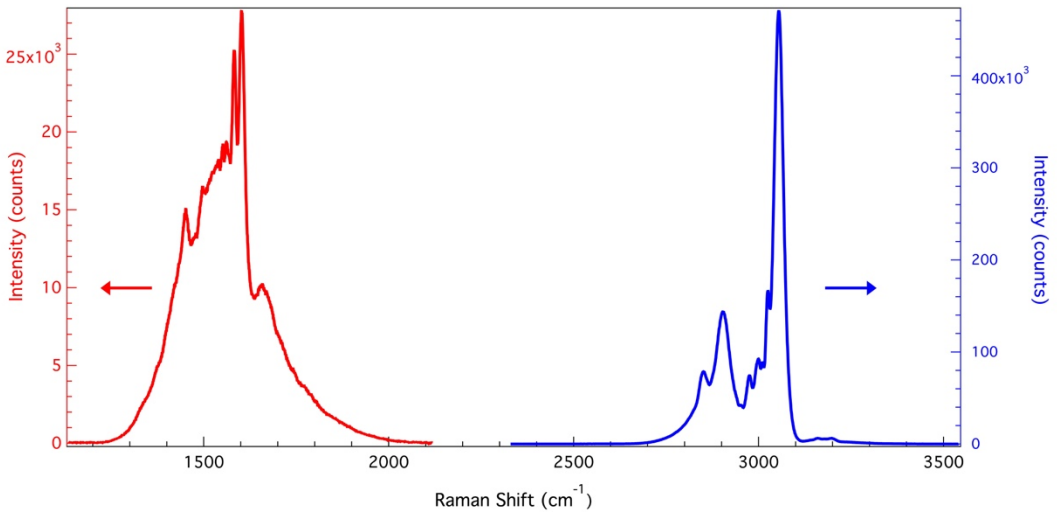

Figure 3.5: CARS spectrum of polystyrene taken with 800 nm CARS pump.

some groups use different polarizations for the input pulses and a polarizer after the sample to minimize the non-resonant background, this approach decreases the intensity of the resonant CARS signal and so is not always optimal [1]. In this work, the input pulses were always of the same polarization. When pumping with 400 nm, both CARS pulses were both *p* polarized, while when pumping with 800 nm, the pulses were both *s* polarized.

The temporal overlap of the three pulses was found using the sum frequency generation (SFG) signals generated from a ZnSe window. Initially, the SFG signals generated by the melting pulse and pump pulse, and by the melting pulse and Stokes pulse are found to determine an approximate time-zero. The time-zero was refined using the resonant CARS signal from highly ordered pyrolitic graphite (HOPG).

3.3. Standard CARS Spectra

Before studying graphite and liquid carbon, the CARS spectra of some standard samples

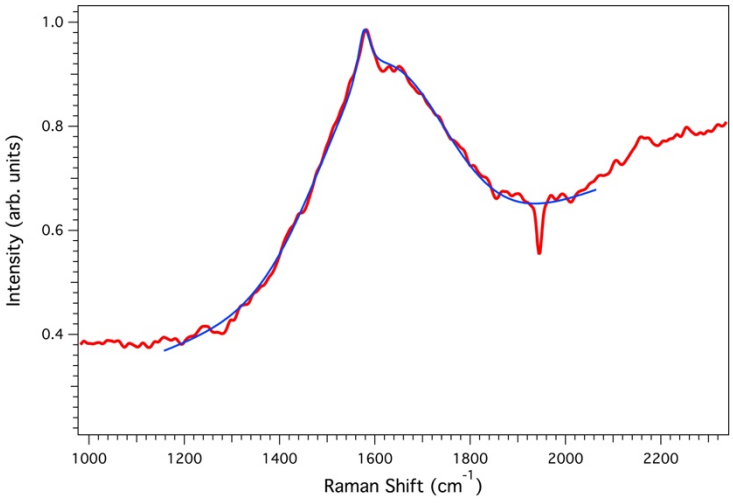

Figure 3.6: CARS spectrum of polystyrene with 400 nm CARS pump.

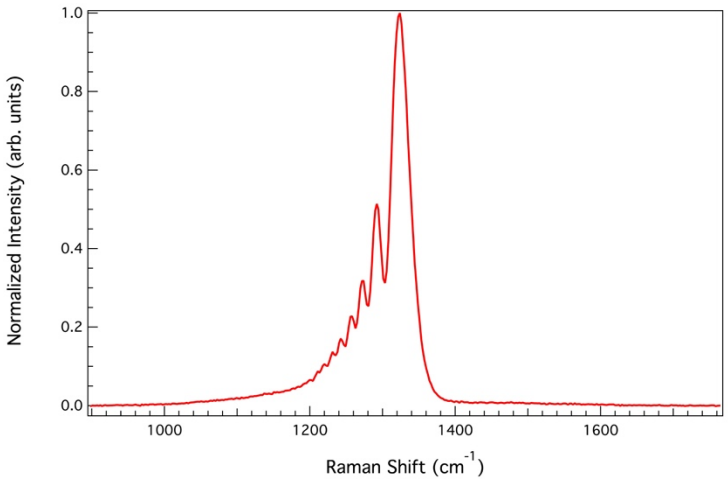

Figure 3.7: CARS spectrum of single crystalline diamond with 400 nm CARS pump.

were taken. Polystyrene is a Raman spectroscopy standard that has prominent resonant peaks around 1600 cm^{-1} near the graphite G peak. The CARS spectrum of a 38 μm thick polystyrene film (International Crystal Laboratories) is shown in Figure 3.5. Two different Stokes wavelengths, 1050 nm and 910 nm, were used with the 800 nm CARS pump to obtain the Raman spectrum in the regions near 3000 cm^{-1} and 1600 cm^{-1} respectively. The two peaks at 1582 cm^{-1} and 1602 cm^{-1} have widths of 10 and 13 cm^{-1} which agree well with literature values [4]. The resonances are less intense at 1600 cm^{-1} and the non-resonant background can be seen clearly. With a 400 nm CARS pump, only one resonance peak is apparent in the polystyrene spectrum at 1600 cm^{-1} (Fig. 3.6). This is likely because the sample is nearly two-photon resonant with the 400 nm pulse (polystyrene absorbs at 260 nm). The two-photon resonance is part of the non-resonant CARS signal, which is much stronger relative to the resonances than it is when using an 800 nm pump pulse [5].

Figure 3.7 shows the CARS spectrum of single crystalline diamond using a 400 nm CARS pump. The 1332 cm^{-1} resonant peak is clearly shown. The peak width is 2 cm^{-1} which is too narrow to be resolved with a 1.86 ps chirped pump pulse [6]. Indeed, the ringing peaks on

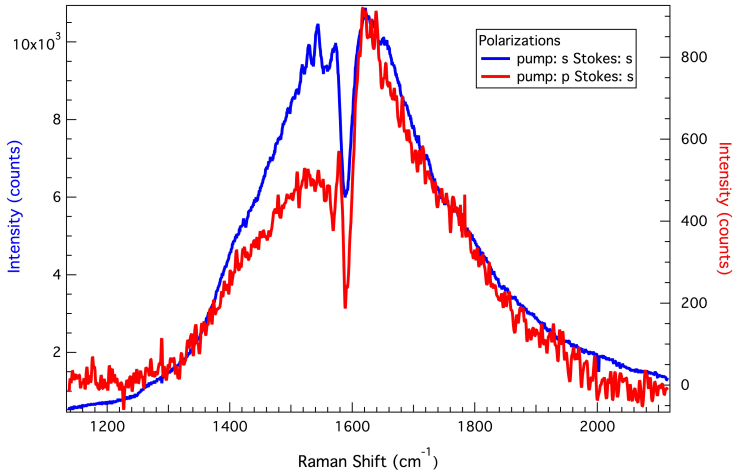

Figure 3.8: CARS spectrum of HOPG with 800 nm CARS pump and two different polarization schemes.

the red side of the resonance are due to interactions between the dephasing of the vibrational mode and the later (red) part of the chirped pump pulse [3].

3.4. CARS Spectra of Graphite and Glassy Carbon

3.4.1. CARS Spectra with an 800 nm CARS pump

Two different carbon samples were studied with CARS. The first, highly ordered pyrolitic graphite (HOPG) (SPI grade-2, SPI supplies), has a density of 2.27 g/cm^3. This sample is best suited for the nonthermal melting experiments because the surface can be exfoliated with a piece of tape to expose undamaged graphite. The second sample was glassy carbon (Sigradur G, HTW GmbH), with a Fullerene like microstructure and a density of 1.42 g/cm^3. This sample surface is smoother than that of the HOPG, but the surface cannot easily be refreshed once it is damaged. The HOPG CARS spectrum is shown in Figure 3.8. The G

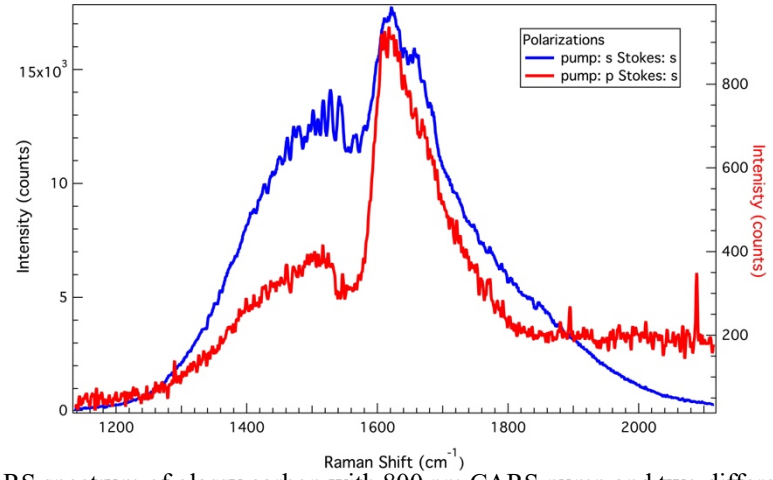

Figure 3.9: CARS spectrum of glassy carbon with 800 nm CARS pump and two different polarization schemes.

peak resonance seen at 1580 cm^{-1} is a negative peak. This resonance is due to the relative motion of the sp^2 carbons in graphite [7]. Because of interactions between the resonant and non-resonant CARS, the peak appears as a negative peak or, in the case of the perpendicular input polarizations, as a derivative peak. As discussed previously, both the non-resonant and resonant signals are orders of magnitude larger with parallel input polarizations than with perpendicular input polarizations. However, the non-resonant and resonant signals do not decrease by the same amount when the polarization is changed, which results in a different peak shape for the resonance. The width of the peak is 20 cm^{-1} which agrees well with literature values from Raman scattering experiments [8]. The CARS spectrum of glassy carbon is shown in Figure 3.9. Again, interactions between the resonant and non-resonant components of the spectrum have caused the resonance to have a derivative-like shape.

3.4.2. CARS Spectra with a 400 nm CARS pump

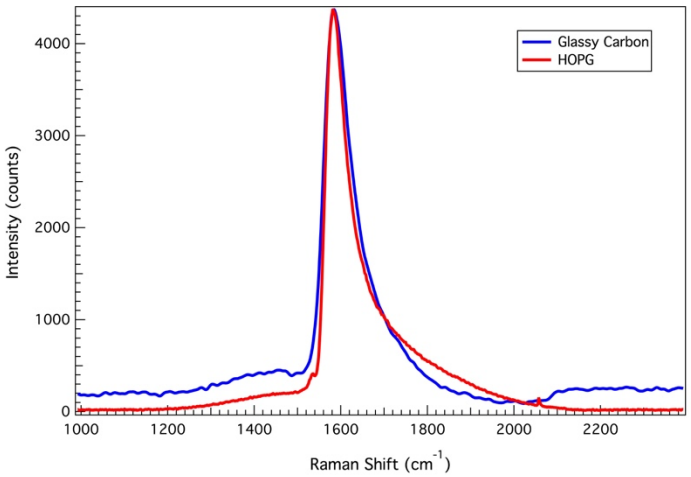

Figure 3.10: CARS spectra of glassy carbon and HOPG with 400 nm CARS pump.

The CARS spectra of HOPG and glassy carbon taken with a 400 nm CARS pump are shown in Figure 3.10. The G peak is much more prominent in this case than with the 800 nm CARS pump. However, the peak FWHM is 65 cm^{-1} over two times the linewidth from Raman scattering measurements. Knutsen et al. [3], showed that the effective CARS resolution should be less than the intrinsic linewidth for a peak to be well-resolved, and so, it was expected that the 20 cm^{-1} wide G peak would be resolved using the 1.86 ps chirped pump pulse. Additionally, the peak has an asymmetric shape in both the HOPG and glassy carbon spectra. Shifting the input Stokes energy does seem to affect this asymmetry (Fig. 3.11), suggesting it is due to an interaction between the resonant and non-resonant components of the CARS signal. The spectra were not normalized by the non-resonant signal because slight changes in alignment and energy calibration can lead to very different normalized spectra. Simulations of the CARS spectrum generated by a 1.86 ps chirped pump pulse, performed using previously developed code, show a linewidth of 44 cm^{-1} indicating that some of the broadening is due to the CARS spectral resolution (Fig. 3.12) [2]. However, the simulation does not capture the asymmetric shape seen in these experiments.

It should be noted that, with a negatively chirped CARS pump, any interactions with the

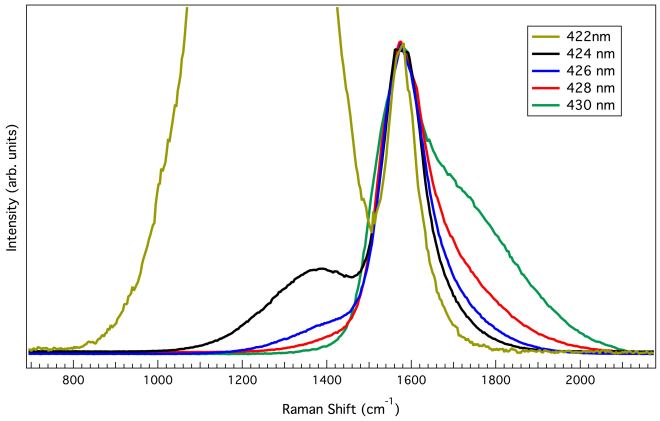

Figure 3.11: CARS spectra HOPG G peak when pumped at different Stokes wavelengths. The spectra have been normalized to the G peak.

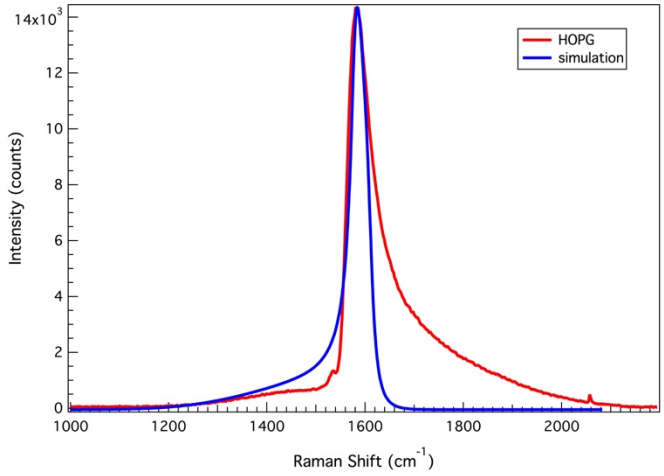

Figure 3.12: CARS spectra HOPG G peak and a simulation of the CARS spectrum.

later part of the chirped pulse would result in ringing peaks at energies lower than the resonance, which is not what is seen in the G peak shape.

In Raman scattering experiments, the other prominent resonance is the D peak, at 1350 cm^{-1} which corresponds to a ring-breathing vibrational mode [7]. Because of symmetry constraints, this mode is non-existent in the spectrum of perfect graphite, but as the sample is damaged (disordered), this mode appears. No D peak is apparent in the HOPG and glassy carbon spectra. This peak is seen in the Raman scattering spectra of these samples (Fig 3.13), but not in the CARS spectrum. As this mode is due to scattering of the excited electron from a defect or phonon mode, it could be that the stimulated emission and de-excitation of the electron occurs instantaneously in CARS and there is no time for scattering to occur.

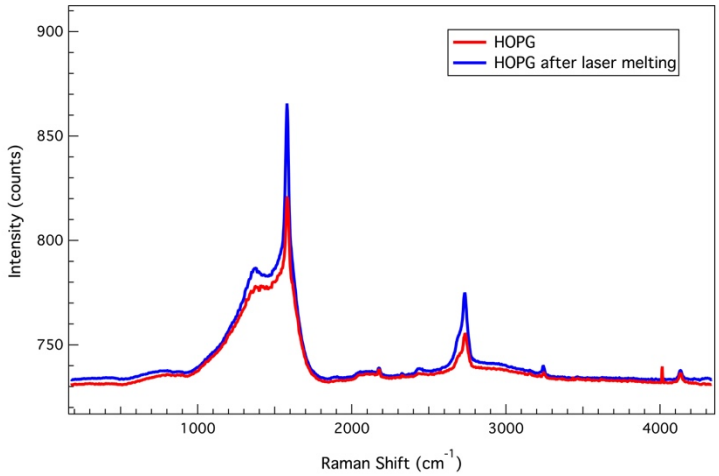

Figure 3.13: Raman scattering spectrum of HOPG before and after melting. The pump wavelength was 488 nm. The sample was melted with a single 800 nm, 90 fs laser pulse with a fluence of 0.56 J/cm^2 (6.2 x 10^{12} W/cm^2 intensity).

3.5. CARS of Non-thermally Melted HOPG

The HOPG sample was melted with an 800 nm, 90 fs ultrafast laser pulse, similar to what was used in previous works [9,10]. Melting fluences from 0.40 to 0.85 J/cm^2 (intensities of 4.4 x 10^{12} to 9.4 x 10^{12} W/cm^2) were chosen so as to be above the melting threshold, but not so high as to directly vaporize the sample. The CARS spectrum at different time delays after melting is shown in Figure 3.14. Figure 3.14a shows delay times below 1.5 ps after melting and Figure 3.14b shows delay times up to 20 ps. The melting fluences used here, 0.40 to 0.45 J/cm^2 (intensities of 4.4 x 10^{12} and 5.0 x 10^{12} W/cm^2), are comparable to those used in visible and UV reflectivity experiments [10,11], but some experiments use fluences up to 2 J/cm^2 (150 fs, 800 nm; 1.3 x 10^{13} W/cm^2 intensity) [9]. It was expected that the G peak would broaden and shift as the material is disordered and becomes a fluid, but no change in the G peak position or width was ever observed. There is only a decrease in intensity over time, likely due to roughening of the surface and formation of a crater. No significant differences in the spectra were seen with melting fluences up to 0.85 J/cm^2 (9.4 x 10^{12} W/cm^2) in and time delays up to 100 ps. Even the damage caused to a single spot on the sample by multiple melting pulses showed the same G peak position and width. A lower energy region of the Raman spectrum, centered about ~1100 cm^{-1} was also studied, to see if any resonant features formed after melting, but again there was only a decrease in non-resonant CARS signal as the sample is damaged.

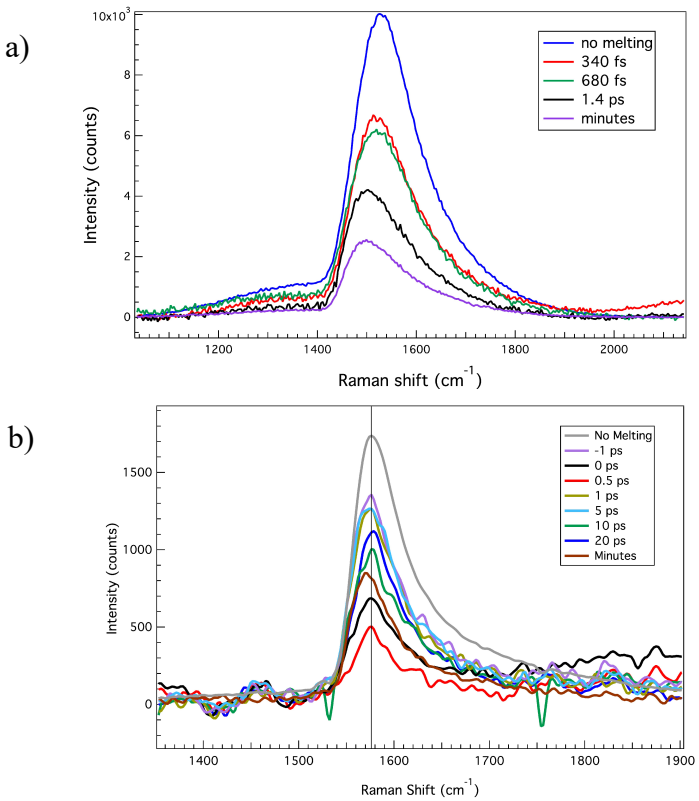

Figure 3.14: CARS spectrum of HOPG after melting. The melting fluences were 0.45 J/cm^2 (5.0 x 10^{12} W/cm^2 intensity) (a) and 0.40 J/cm^2 (4.4 x 10^{12} W/cm^2 intensity) (b).

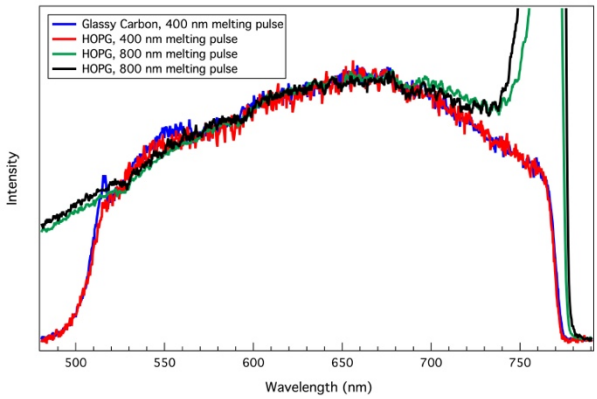

Figure 3.15: Background generated by the melting pulse at two different melting wavelengths and two different samples.

Studies of liquid carbon were also attempted using an 800 nm CARS pump, but the background generated by the melting pulse was very large and no signal could be discerned. This was the case at all delay times as the CCD camera sums multiple laser shots in each image, with a minimum exposure time of 10 ms. Therefore, the average background from the melting pulse is always captured in the image, regardless of the delay time between the melting and probe pulse. This melting background was also seen in the spectra with a 400 nm CARS pump, but the signal to background ratio was still large enough to be observed. Irises and filters after the sample were used to minimize this background, but could not eliminate it completely. The background from the melting pulse appears independent of the sample and the wavelength of the melting pulse (3.15). It peaks at 650 nm, which, if we treat this background as black body emission, would correspond to a temperature of 4500 K, in the range of temperatures expected for liquid carbon. However, the shape of the melting pulse background does not match the functional form of black body emission, and is likely affected by other photoemission processes, including nonlinear processes. It should also be noted that the background spectrum shown is the average over many seconds and instantaneous temperatures will be different from what is calculated here.

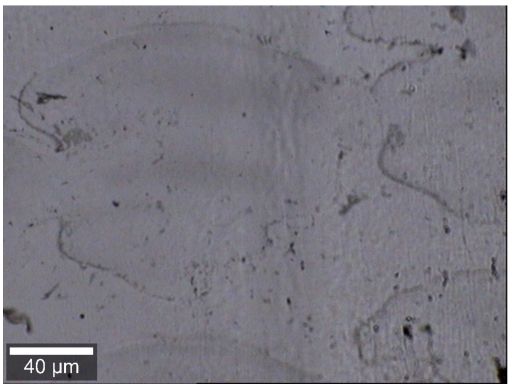

Figure 3.16: Microscope image of the damage on a HOPG sample from a 0.40 J/cm^2, 800 nm, 90 fs melting pulse.

In order to ensure we are damaging the sample, microscope images of the HOPG were taken (Fig. 3.16). The damage spot can be clearly seen, and no damage is seen from the CARS pulses. It is unclear why the CARS spectrum remains unchanged. It could be that only a small portion of the probe area is melted and so the signal is primarily from unmelted carbon. However, the fluences used are well above reported thresholds and the delay times probed were comparable to those studied by others.

3.6. References

[1] C. L. Evans and X. S. Xie, Annu. Rev. Anal. Chem. **1**, 883 (2008).
[2] K. P. Knutsen, Chirped Femtosecond Coherent Anti-Stokes Raman Scattering Spectromicroscopy, University of California, Berkeley, 2005.
[3] K. P. Knutsen, B. M. Messer, R. M. Onorato, and R. J. Saykally, J. Phys. Chem. B **110**, 5854 (2006).
[4] W. M. Sears, J. L. Hunt, and J. R. Stevens, J. Chem. Phys. **75**, 1589 (1981).
[5] J. Cheng, A. Volkmer, L. D. Book, and X. S. Xie, J. Phys. Chem. B **105**, 1277 (2001).
[6] S. A. Solin and A. K. Ramdas, Phys. Rev. B **1**, 1687 (1970).
[7] A. C. Ferrari and J. Robertson, Phys. Rev. B **61**, 14095 (2000).
[8] Y. Wang, D. C. Alsmeyer, and R. L. McCreery, Chem. Mater. **2**, 557 (1990).
[9] S. L. Johnson, P. A. Heimann, A. G. MacPhee, A. M. Lindenberg, O. R. Monteiro, Z. Chang, R. W. Lee, and R. W. Falcone, Phys. Rev. Lett. **94**, (2005).
[10] R. Mincigrucci, E. Giangrisostomi, E. Principi, A. Battistoni, F. Bencivenga, R. Cucini, A. Gessini, M. Izzo, and C. Masciovecchio, Photonics **2**, 50 (2015).
[11] D. H. Reitze, H. Ahn, and M. C. Downer, Phys. Rev. B **45**, 2677 (1992).

Chapter 4: Soft X-ray Second Harmonic Generation

To further our studies of liquid carbon, X-ray techniques were explored, as they would provide information on the electronic structure of the material that would complement our visible and UV studies. Of particular interest was soft X-ray second harmonic generation, that can be used to elucidate the electronic structure of liquid carbon and also study solid-solid interfaces that are difficult to probe with other techniques.

4.1. Soft X-Ray Second Harmonic Generation from Graphite

 Sumana Raj worked with Royce Lam to carry out the experiment and data analysis, and assisted in the writing of the paper.

Full citation: Lam, R. K.; Raj, S. L.; Pascal, T. A.; Pemmaraju, C. D.; Foglia, L.; Simoncig, A.; Fabris, N.; Miotti, P.; Hull, C. J.; Rizzuto, A. M.; et al. Soft X-Ray Second Harmonic Generation as an Interfacial Probe. *Phys. Rev. Lett.* **2018**, *120* (2), 023901. https://doi.org/10.1103/PhysRevLett.120.023901.

Nonlinear optics has recently been extended from visible and near UV wavelengths to new regimes with the development of x-ray free electron lasers (XFELs) capable of delivering x-ray pulses with high brightness, ultrashort pulse duration, and high coherence [1–7]. One fundamental nonlinear probe is second harmonic generation (SHG), a second-order process which combines two photons of the same energy to generate a single photon with twice the energy [8]. At infrared, visible, and ultraviolet wavelengths, second-order nonlinear spectroscopies have become important tools in surface science, as symmetry considerations within the dipole approximation constrain signal generation to regions lacking centrosymmetry, such as surfaces and interfaces [9–12]. In contrast, at hard x-ray wavelengths, second harmonic and sum frequency generation (SFG) have been observed in centrosymmetric materials with a nonuniform electron density and are essentially bulk probes [1,2]. As soft x-ray wavelengths fall in between the hard x-ray and UV regimes, there has been uncertainty regarding the interface specificity of soft x-ray SHG. Here, by utilizing a recently constructed, highly coherent, soft x-ray free electron laser [13,14], we report the first observation of soft x-ray second harmonic generation near the carbon K edge (~284 eV). Our experimental results and accompanying theoretical analysis indicate that soft x-ray SHG is an interface-specific probe with symmetry constraints similar to optical SHG or SFG, and is highly sensitive to resonance effects. This enables a powerful new approach for surface and interface analysis with broad applicability to many scientific fields, as it combines the elemental and chemical specificity of x-ray absorption spectroscopy with the rigorous interfacial specificity of second-order nonlinear spectroscopies, while maintaining a fully coherent signal. With several new coherent free electron lasers under development (SwissFEL, SXFEL, LCLS-II, FLASH2020) [15,16], this new technique offers exciting applications to a wide range of problems.

At optical wavelengths, second-order nonlinear spectroscopies have become indispensable techniques for surface analysis, being among the few techniques with genuine interface

specificity. As such, SHG and SFG have been employed to study of a wide range of scientifically important systems (e.g., liquid-vapor interfaces, catalytic interfaces, etc.) [11]. These techniques exploit the enhancement of the second-order nonlinear response to a high intensity, coherent photon beam when either the intermediate or final state is resonant with a real state within the target material. The nonlinear response to a coherent input beam of frequency can be derived from an expansion of the polarization of the target medium

$$P = \chi^{(1)}E + \chi^{(2)}EE + \chi^{(3)}EEE + \cdots \quad (1)$$

where $\chi^{(n)}$ is the nth-order susceptibility tensor. Within the dipole approximation, even orders of $\chi^{(n)}$ necessarily vanish in centrosymmetric media. This causes SHG, SFG, difference frequency generation, and higher even-order nonlinear signals to be inherently surface specific in centrosymmetric media, as this symmetry is broken only at interfaces. Assuming a broken-symmetry region with thickness much less than the wavelength, the intensity of the SHG signal from a given interface is given by

$$I_{2\omega} \propto |\chi^{(2)}_{eff}|^2 I_\omega^2 \quad (2)$$

where $\chi^{(2)}_{eff}$ is the effective susceptibility of the interfacial region, and I_ω is the intensity of the fundamental beam. Note the quadratic dependence of the second harmonic (SH) intensity $I_{2\omega}$ on the input intensity I_ω.

Until recently, the lack of light sources with sufficient intensity and coherence has limited the development of nonlinear x-ray spectroscopies. Prior to the development of free electron lasers (FELs), only parametric down-conversion had been observed [17]. While the advent of XFELs has recently enabled second- and third-order nonlinear spectroscopies at hard x-ray energies, including SHG [2], SFG [1], two-photon absorption [4], and inelastic Compton scattering [18], current hard x-ray FELs lack the longitudinal and temporal coherence necessary for efficiently satisfying the phase-matching conditions required for nonlinear spectroscopies, thus, making the exploitation of some of these techniques difficult [19,20]. Furthermore, the shorter hard x-ray wavelengths (λ<0.2 nm) induce second harmonic and sum frequency generation even within centrosymmetric media, as the observed response depends on material inhomogeneity on the length scale of the x-ray wavelength, similar to how SHG is seen in a plasma, and effectively making this method a bulk probe [21].

4.1.1. Experimental Details

Here we report the observation of soft x-ray SHG generated by high intensity, coherent FEL pulses at FERMI, a highly coherent soft x-ray FEL based on high-gain harmonic generation of a longer wavelength seed laser [13,14]. The experiments were conducted at the EIS-TIMEX end station [22,23]. An experimental schematic is shown in Fig. 4.1(a): a soft x-ray FEL pulse (estimated pulse duration ~25 fs, pulse energy ~1–5 μJ, spot size ~350 μm^2; intensities of 1–6 x 10^{13} W/cm^2) is passed through a 2 mm iris to attenuate the off-axis second harmonic contamination from the FEL source and focused onto a graphite sample at normal incidence. The transmitted beam and the collinear SH signal are passed through a 600 nm aluminum filter to attenuate the fundamental FEL pulse into a spectrograph [24] to separate the SH signal from the fundamental, and onto a CCD detector [Fig. 4.1(b)]. The sample was raster scanned so that pristine graphite was probed with each laser pulse. Measurements were made using three discrete wavelengths chosen to have incoming photon energies lying below (λ=4.76 nm, $\hbar\omega$=260 eV)

on (λ=4.36 nm, ħω=284 eV), and above (λ=4.02 nm, ħω=308 eV) the carbon K-edge absorption edge of graphite [see Fig. 4.1(c)] to demonstrate the effects of resonant enhancement. In this case, the FEL energy is resonant with the intermediate state and generates a nonresonant signal enabling transmission experiments. SHG spectra can also be measured at half the photon energy used here, where the final state is resonant, although this would hinder transmission studies. Measurements were made both with and without the sample present to permit subtraction of any remaining second harmonic contamination from the FEL beam. See the Supplemental Material for additional details on the experimental design and analysis procedures [25].
The measured dependence of the second harmonic signal on the pulse energy for multiple

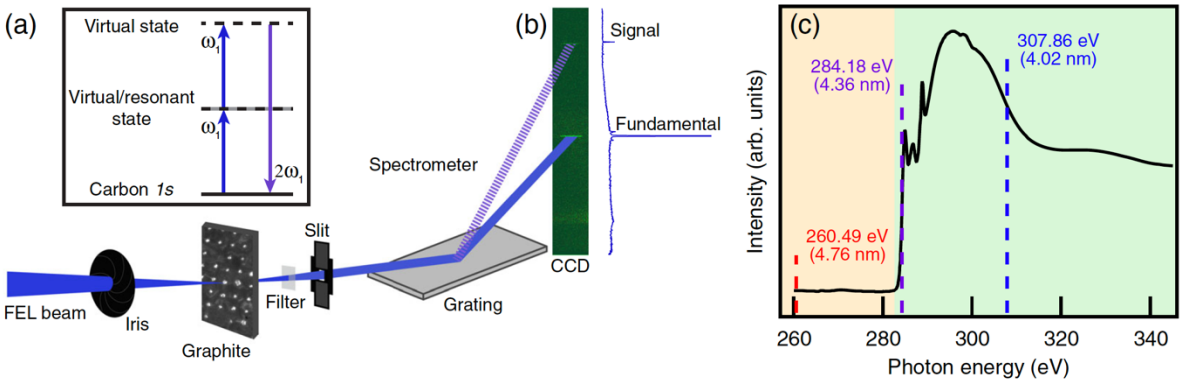

Figure 4.1: Experimental design. (a) X-ray pulses are passed through a 2 mm iris, then focused by an ellipsoidal mirror (not shown) onto the graphite sample (spot size ~350 μm2) at normal incidence. The transmitted beam and the collinear second harmonic signal (double the fundamental photon energy) are passed through a 600 nm aluminum filter and into a spectrometer, spatially separating the second harmonic signal from the fundamental. A schematic energy level diagram of the SHG process is shown in the inset. (b) The CCD image and projection of the transmitted FEL beam and the SHG signal for a single FEL pulse. (c) Linear, total electron yield x-ray absorption spectrum of a 500 nm graphite sample. X-ray SHG measurements were made at the three discrete photon energies (ω1) shown in the dashed lines. The nonresonant (below the C K edge) and resonant (above the C K edge) regions are shaded in orange and green, respectively.

thicknesses of graphite (100–720 nm) corresponding to 260, 284, and 308 eV is shown in Figs. 4.2(a), 4.2(b), and 4.2(c), respectively. The pulse energy was calculated from the absolute number of x-ray photons incident on the sample, which was directly measured by the spectrometer with the sample removed. A quadratic fit to the SH response with respect to input intensity at a given photon energy is represented by a dashed line. At each photon energy, the power dependence of the SH signal is largely invariant with the sample thickness, an observation that is consistent with surface sensitivity in a centrosymmetric sample. Notably, even for thin samples with a large transmission (>70%), a thickness-dependent increase in the SH signal is not observed, implying that the signal is not bulk-volume dependent. This invariance with sample thickness is also observed at resonant photon energies. The bulk second harmonic signal in graphite due to electric quadrupole contributions is weak.

4.1.2. Discussion

At the resonant photon energies, a significant enhancement of the SH signal was observed, permitting its detection with significantly lower pulse energies. The tunable nature of FELs facilitates resonance and double resonance exploitation. The relative $\left|\chi_{eff}^{(2)}\right|^2$ response of graphite at different x-ray wavelengths is proportional to the slope of the linearized power dependence curve (SH response vs [input power]^2) shown in Fig. 4.2(d). A significant enhancement in the $\left|\chi_{eff}^{(2)}\right|^2$ response is observed when exciting with x-ray energies at or above the graphite absorption onset (>284 eV). In this case, the intermediate state is resonant with discrete transitions to unoccupied electronic states [Fig. 4.1(c)], and the data are consistent with the expected resonant enhancement of the SH signal when either the intermediate or final state is real. When off resonance at 260.49 eV, a threshold pulse energy of over 3 μJ per pulse is required for a sufficient SH signal-to-noise ratio as determined based on the minimum of the quadratic fits shown in Fig. 4.2. On resonance, the pulse energy necessary is significantly lower, viz., 0.7 and 0.3 μJ at 284.18 and 307.86 eV, respectively. This resonance enhancement means that the technique can be used to generate a surface-specific soft x-ray spectrum with sensitivity to chemical composition. The pump intensities used here correspond to peak fields of 1012 W/cm^2, which is 4 orders of magnitude less than what was required for hard x-ray SHG

(1016 W/cm^2) [2]. Note that at these power densities, the efficiency of the SHG process is at least an order of magnitude lower than the linear absorption for a single atomic layer [36].

While the exact damage threshold will vary based on the sample, we expect that it will be possible to perform soft x-ray SFG below the damage threshold for a broad variety of materials by leveraging the lower x-ray fields required by combining the soft x-ray pulse with an optical laser pulse. When hard x-ray SFG was performed by using an optical laser pulse combined with an x-ray laser, the pump intensities were ~1010 W/cm^2 for the optical laser and 1011 W/cm^2 for the x-ray laser [1]. Additionally, as a soft x-ray SHG requires significantly smaller fields than does a hard x-ray SHG, such damage-free SHG measurements may be achievable by exploiting

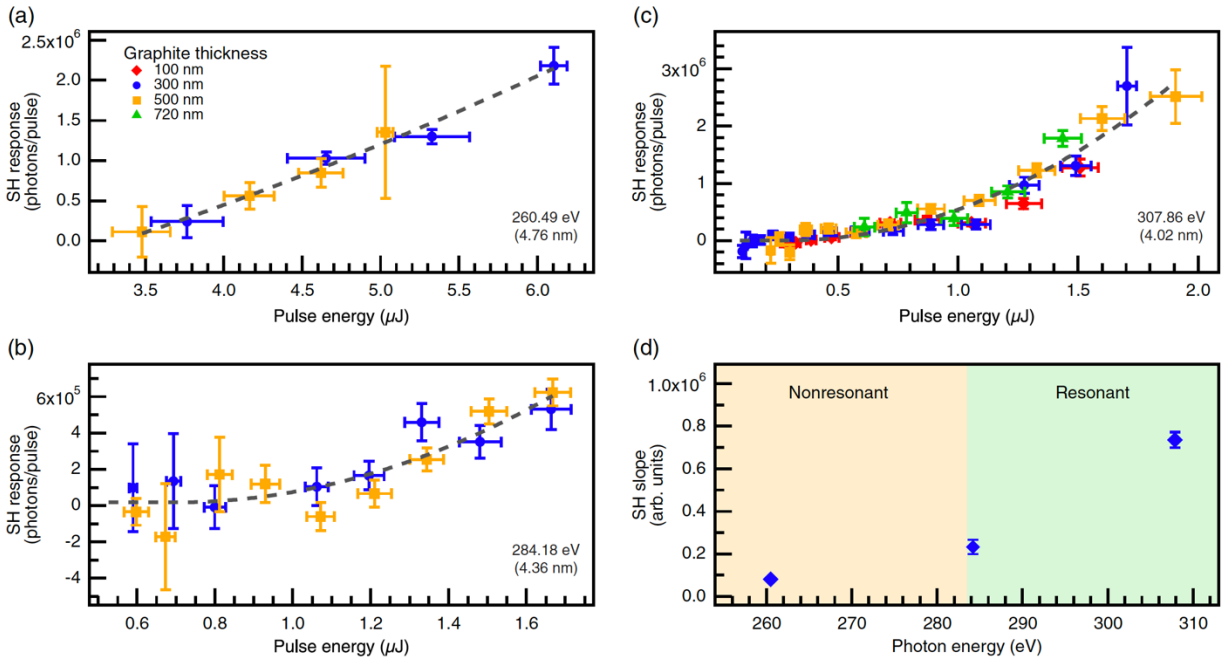

Figure 4.2: Pulse energy dependence of soft x-ray SHG. The second harmonic response at 260.49 (a), 284.18 (b), and 307.86 eV (c) of graphite thin films (100 nm, red diamond; 300 nm, blue circle; 500 nm, orange square; 720 nm, green triangle). The dashed lines represent quadratic fits to all the points at a given photon energy constrained to show no detectable second harmonic signal generated below a threshold pulse energy. The vertical and horizontal error bars represent the standard error of the SH response and the standard deviation of the pulse energies in each bin, respectively. (d) The slope of the linearized pulse energy dependence curve for each photon energy. The relative $\left|\chi_{eff}^{(2)}\right|^2$ response is proportional to the slope of the linearized pulse energy dependence curve (SH response vs [input power]^2). Error bars represent the standard deviation from the linear regression analysis. The nonresonant and resonant regions are shaded in orange and green, respectively.

higher repetition rate FELs (LCLS-II, FLASH2020) and more efficient detection (better spectrometer, spatial separation, etc.).

In order to verify our experimental observation of a significant SHG response in the soft x-ray regime of graphite, we calculated the linear and second-order response from first principles using perturbation theory within density functional theory [37,38]. This approach is broadly applicable for calculating electronic SHG and SFG spectra from the optical regime through the x-ray energies and is detailed in the Supplemental Material [25]. Figures 4.3(a) and 4.3(b) present the linear and SH response, respectively, of an eight-layer slab of AB stacked hexagonal graphite. A

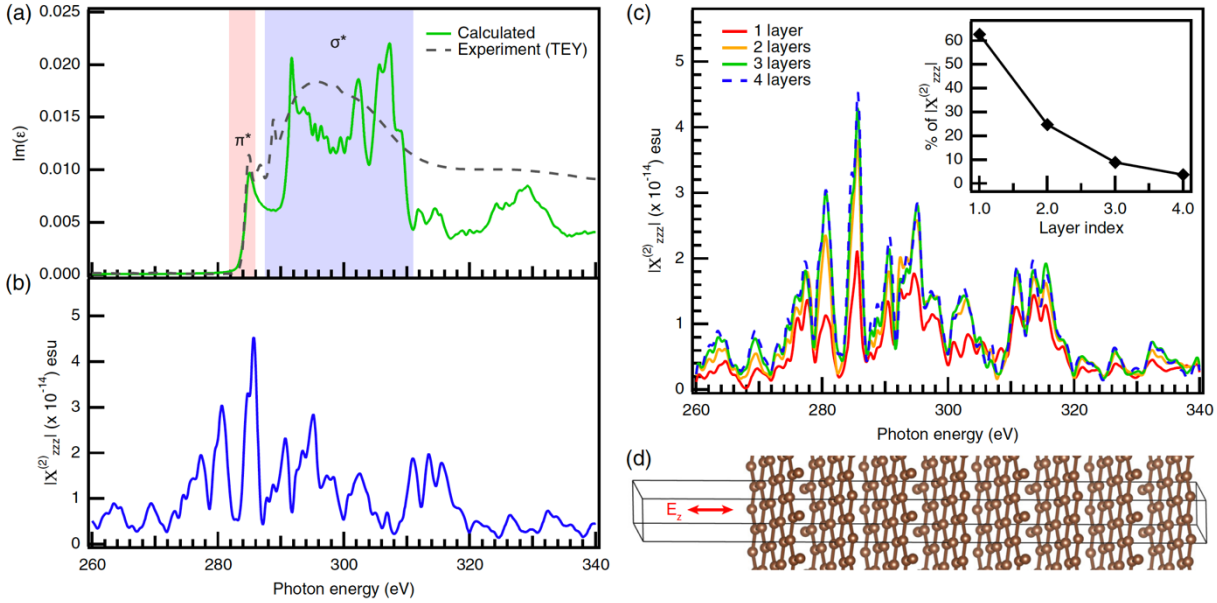

Figure 4.3: Second harmonic susceptibility from first-principles theory. (a) Imaginary part (green solid) of the linear dielectric function corresponding to the calculated linear spectrum at the C K-edge NEXAFS region calculated with a density-functional-theory-based supercell approach for an eight-layer slab of graphite compared with the experimental linear spectrum (gray, dashed). The π* and σ* transitions are labeled in red and blue, respectively. The experimental peak between the marked π* and σ* regions corresponds to oxidized graphite. Note that a more realistic comparison between theory and experiment can be obtained by sampling a finite temperature molecular dynamics simulation as inhomogeneity in thermalized samples is a significant contributor to spectral broadening. (b) Calculated C 1s core level contribution to the magnitude $\left|\chi^{(2)}_{zzz}\right|$ of the *zzz* component of the second-order nonlinear susceptibility tensor $\chi^{(2)}(2\omega,\omega,\omega)$. relevant to SHG near the C K edge of a graphite surface. C 1s core levels from the top four surface layers of an eight-layer slab of graphite [shown in (d)] are considered in the simulation. The z axis is perpendicular to the surface of the slab. (c) Convergence of the calculated $\left|\chi^{(2)}_{zzz}\right|$ as a function of the number of surface layers whose C 1s core states are included in the simulation. The inset shows the percentage contribution to $\left|\chi^{(2)}_{zzz}\right|$ from each of the top four individual layers obtained by integrating $\left|\chi^{(2)}_{zzz}\right|$ over a 260–340 eV energy window plotted as a function of the layer index. Contribution to the overall response is seen to decay exponentially moving into the bulk of the slab with the top layer accounting for ~63% of the signal. (d) Periodic supercell of the eight layer graphite slab employed in the simulations.

better comparison to experiments can be obtained by sampling a finite temperature molecular dynamics trajectory, as has been demonstrated for linear absorption [39]. Nevertheless, the linear absorption spectrum calculated here within the independent particle approximation captures salient resonant features, such as π∗ and σ∗ features at 284.9 and 291.65 eV, compared to the respective experimental values of 284.9 and 288.8 eV. Because of symmetry considerations, only the χ_{zzz} component of the $\chi^{(2)}$ susceptibility tensor is nonvanishing. Small changes in the energy

calibration and temperature effects in the theory and the imperfect materials used in the experiments can engender large differences in signal intensity, particularly near the absorption edge, likely accounting for the observed differences between experiment and theory. The main features in the SH spectrum correspond to excitations from a convolution of the ground state and π^* and σ^* intermediate states in the conduction band. As such, a direct comparison between the SH spectrum and the linear spectrum is infeasible.

The signal originating from each layer of the graphite slab was isolated in order to determine the exact degree of surface specificity. As shown in the inset of Fig. 4.3(c), the contribution to the overall response decays exponentially as a function of the layer index and is essentially limited to the first three monolayers, or ~0.5 nm, with ~63% of the signal originating from the topmost layer, ~25% from the second, and ~9% from the third. This result is consistent with expectations from optical sum frequency generation, wherein 90% of the signal originates from the first two molecular layers [40].

In conclusion, soft x-ray second harmonic generation is demonstrated to be a powerful elemental- and chemical-specific spectroscopy that is highly symmetry sensitive. More specifically, the interfacial nonlinearity is large enough to prevail over the plasma nonlinearities that are dominant at hard x-ray wavelengths. This new technique will permit a new class of interface analysis experiments with significantly higher interfacial specificity than existing soft x-ray methods, effectively allowing for x-ray absorption spectroscopy of the first few molecular layers of an exposed bulk sample or either side of a buried interface. For example, buried interfaces in layered samples, wherein an individual layer contains an element not present in the others, could be probed directly without concomitant contamination from the exposed interfaces. Additionally, as the pulses remain fully coherent, it should be possible to combine this technique with lensless coherent imaging techniques with a resolution not limited by aberration [41]. Such a technique would require either an energy-sensitive nondispersive detector or the generation of a signal that is spatially separated from the input pulses, as has been achieved previously with noncollinear input laser pulses, such as in optical SFG [9–12]. If radiation damage concerns can be mitigated, the spectral sensitivity demonstrated here would enable experiments which can both spectroscopically and spatially resolve nanoparticles. Such measurements, when combined with the first-principles electronic structure framework developed here, will have broad applicability to a variety of systems of current interest.

4.1.3. References

[1] T. E. Glover, D. M. Fritz, M. Cammarata, T. K. Allison, S. Coh, J. M. Feldkamp, H. Lemke, D. Zhu, Y. Feng, R. N. Coffee, M. Fuchs, S. Ghimire, J. Chen, S. Shwartz, D. A. Reis, S. E. Harris, and J. B. Hastings, Nature (London) **488**, 603 (2012).

[2] S. Shwartz, M. Fuchs, J. B. Hastings, Y. Inubushi, T. Ishikawa, T. Katayama, D. A. Reis, T. Sato, K. Tono, M. Yabashi, S. Yudovich, and S. E. Harris, Phys. Rev. Lett. **112**, 163901 (2014).

[3] N. Rohringer, D. Ryan, R. A. London, M. Purvis, F. Albert, J. Dunn, J. D. Bozek, C. Bostedt, A. Graf, R. Hill, S. P. Hau-Riege, and J. J. Rocca, Nature (London) **481**, 488 (2012).
[4] K. Tamasaku, E. Shigemasa, Y. Inubushi, T. Katayama, K. Sawada, H. Yumoto, H. Ohashi, H. Mimura, M. Yabashi, K. Yamauchi, and T. Ishikawa, Nat. Photonics **8**, 313 (2014).
[5] F. Bencivenga, F. Capotondi, R. Mincigrucci, R. Cucini, M. Manfredda, E. Pedersoli, E. Principi, A. Simoncig, and C. Masciovecchio, Phys. Scr. **T169**, 014003 (2016).
[6] F. Bencivenga, R. Cucini, F. Capotondi, A. Battistoni, R. Mincigrucci, E. Giangrisostomi, A. Gessini, M. Manfredda, I. P. Nikolov, E. Pedersoli, E. Principi, C. Svetina, P. Parisse, F. Casolari, M. B. Danailov, M. Kiskinova, and C. Masciovecchio, Nature (London) **520**, 205 (2015).
[7] J. Szlachetko, J. Hoszowska, J.-C. Dousse, M. Nachtegaal, W. Błachucki, Y. Kayser, J. Sà, M. Messerschmidt, S. Boutet, G. J. Williams, C. David, G. Smolentsev, J. A. van Bokhoven, B. D. Patterson, T. J. Penfold, G. Knopp, M. Pajek, R. Abela, and C. J. Milne, Sci. Rep. **6**, 33292 (2016).
[8] P. A. Franken, A. E. Hill, C. W. Peters, and G. Weinreich, Phys. Rev. Lett. **7**, 118 (1961).
[9] K. B. Eisenthal, Annu. Rev. Phys. Chem. **43**, 627 (1992).
[10] A. M. Rizzuto, S. Irgen-Gioro, A. Eftekhari-Bafrooei, and R. J. Saykally, J. Phys. Chem. Lett. **7**, 3882 (2016).
[11] Y.-R. Shen, *Fundamentals of Sum-Frequency Spectroscopy* (Cambridge University Press, Cambridge, England, 2016).
[12] H.-F. Wang, W. Gan, R. Lu, Y. Rao, and B.-H. Wu, Int. Rev. Phys. Chem. **24**, 191 (2005).
[13] E. Allaria *et al.*, Nat. Photonics **6**, 699 (2012).
[14] E. Allaria *et al.*, Nat. Photonics **7**, 913 (2013).
[15] J. Galayda, Linac14, Geneva, Switzerland, http://accelconf.web.cern.ch/AccelConf/linac2014/, 2014.
[16] M. Song, C. Feng, D. Huang, H. Deng, B. Liu, and D. Wang, Nucl. Sci. Tech. **28**, 90 (2017).
[17] S. Shwartz, R. N. Coffee, J. M. Feldkamp, Y. Feng, J. B. Hastings, G. Y. Yin, and S. E. Harris, Phys. Rev. Lett. **109**, 013602 (2012).
[18] M. Fuchs *et al.*, Nat. Phys. **11**, 964 (2015).
[19] I. A. Vartanyants *et al.*, Phys. Rev. Lett. **107**, 144801 (2011).
[20] L.-H. Yu *et al.*, Science **289**, 932 (2000).
[21] A. Nazarkin, S. Podorov, I. Uschmann, E. Förster, and R. Sauerbrey, Phys. Rev. A **67**, 041804 (2003).
[22] A. Simoncig, R. Mincigrucci, E. Principi, F. Bencivenga, A. Calvi, L. Foglia, G. Kurdi, L. Raimondi, M. Manfredda, N. Mahne, R. Gobessi, S. Gerusina, C. Fava, M. Zangrando, A. Matruglio, S. Dal Zilio, V. Masciotti, and C. Masciovecchio, Proc. SPIE Int. Soc. Opt. Eng. **10243**, 102430L (2017).
[23] C. Masciovecchio *et al.*, J. Synchrotron Radiat. **22**, 553 (2015).
[24] L. Poletto, F. Frassetto, P. Miotti, A. Di Cicco, P. Finetti, C. Grazioli, F. Iesari, A. Kivimäki, S. Stagira, and M. Coreno, Rev. Sci. Instrum. **85**, 103112 (2014).
[25] See Supplemental Material at http://link.aps.org.libproxy.berkeley.edu/supplemental/10.1103/PhysRevLett.120.023901

for additional details on the experimental design, data analysis procedure, and theoretical methods, which includes Refs. [26–35].
[26] P. Finetti *et al.*, Phys. Rev. X **7**, 021043 (2017).
[27] M. Zangrando, D. Cocco, C. Fava, S. Gerusina, R. Gobessi, N. Mahne, E. Mazzucco, L. Raimondi, L. Rumiz, and C. Svetina, J. Synchrotron Radiat. **22**, 565 (2015).
[28] P. Hohenberg and W. Kohn, Phys. Rev. **136**, B864 (1964).
[29] W. Kohn and L. J. Sham, Phys. Rev. **140**, A1133 (1965).
[30] P. Trucano and R. Chen, Nature (London) **258**, 136 (1975).
[31] N. Ooi, A. Rairkar, and J. B. Adams, Carbon **44**, 231 (2006).
[32] J. P. Perdew and A. Zunger, Phys. Rev. B **23**, 5048 (1981).
[33] S. Klinkusch, P. Saalfrank, and T. Klamroth, J. Chem. Phys. **131**, 114304 (2009).
[34] A. P. Sorini, J. J. Kas, J. J. Rehr, M. P. Prange, and Z. H. Levine, Phys. Rev. B **74**, 165111 (2006).
[35] C. Kunz, B. Cowie, W. Drube, T.-L. Lee, S. Thiess, C. Wild, and J. Zegenhagen, J. Electron Spectrosc. Relat. Phenom. **173**, 29 (2009).
[36] B. L. Henke, E. M. Gullikson, and J. C. Davis, At. Data Nucl. Data Tables **54**, 181 (1993).
[37] S. Sharma and C. Ambrosch-Draxl, Phys. Scr. **T109**, 128 (2004).
[38] A. Gulans, S. Kontur, C. Meisenbichler, D. Nabok, P. Pavone, S. Rigamonti, S. Sagmeister, U. Werner, and C. Draxl, J. Phys. Condens. Matter **26**, 363202 (2014).
[39] J.-J. Velasco-Velez, C. H. Wu, T. A. Pascal, L. F. Wan, J. Guo, D. Prendergast, and M. Salmeron, Science **346**, 831 (2014).
[40] A. Morita and J. T. Hynes, Chem. Phys. **258**, 371 (2000).
[41] J. Miao, P. Ercius, and S. J. L. Billinge, Science **353**, 2157 (2016). aaf.

4.2. Probing Buried Solid-Solid Interfaces with Soft X-ray Second Harmonic Generation

This section contains content submitted to Physical Review Letters. Sumana Raj led the experimental efforts and carried out the data analysis and writing of the paper.

Full Citation: Raj, S. L.; et al. Probing Buried Solid-Solid Interfaces with Soft X-ray Second Harmonic Generation. *Phys. Rev. Lett.* **2019,** *in preparation*.

Surfaces and interfaces play central roles in various biological systems, electronics, batteries, and catalysts. Key chemical reactions and physical processes are dependent on the structure of the interface and the dynamics across it. Currently, surfaces and buried interfaces are often studied using grazing incidence X-ray scattering [1,2], second harmonic generation (SHG) and sum frequency generation (SFG) [3,4], scanning probe techniques [5,6], and total internal reflection spectroscopies [7–9]. However, these techniques are limited in this context because of interactions with the bulk materials (e.g. absorption) that can decrease or obfuscate the signal from the interface.

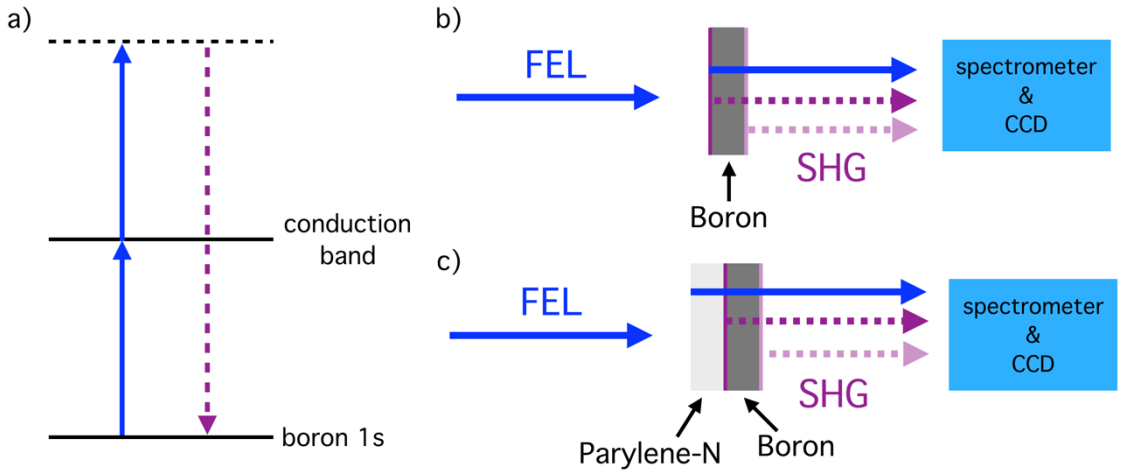

Figure 4.4: Schematic of SHG from interfaces. In the energy level diagram (a), the input FEL energy (solid, blue) is resonant with the boron K-edge. Two photons at this energy combine in the material and a photon at twice the energy (the second harmonic) is emitted (dashed, purple). The SH generated from the boron/vacuum surface of the unsupported boron film (b), and from the buried boron/Parylene-N interface (c) is transmitted and detected with a spectrometer and CCD. The spectrometer separates the fundamental and SHG, and both are detected on the CCD. The FEL pulse is transmitted through the sample and detected, while the SHG only generated by the boron-containing interfaces (purple). The weaker SH signal from the back boron/vacuum interface is shown in the lighter purple.

Soft X-ray SHG offers powerful advantages compared to other surface-specific techniques [10,11]. Linear X-ray absorption spectroscopy (XAS) is a generally useful tool for studying compounds as it is element-specific and sensitive to the coordination environment of the atom [12]. X-rays are highly penetrating, but different detection methods provide a range of depth sensitivities: transmission measurements are bulk-sensitive, fluorescence detection is sensitive to ~ 1 μm based on the penetration of the photons [13], and photoelectron or total electron yield (TEY) detection provides sensitivity of a few nanometers due to the limited escape depth of photoelectrons [14–17]. Even TEY detection cannot match the interfacial sensitivity of SHG in the IR to UV, with signal is only generated from the interface in centrosymmetric media [3,18–20]. For hard (>5 keV) X-ray irradiation, the wavelength is short enough that the electric field is sensitive to inhomogeneities on an atomic scale, and the second harmonic (SH) is generated throughout the material (i.e. it is bulk-sensitive) [21,22]. Soft (<1 keV) X-rays, however, have sufficiently long wavelengths such that SH signal is only generated at interfaces of centrosymmetric media, as shown recently in the first demonstration of soft X-ray SHG [10].

Combining the surface-specificity of visible SHG with the element-specificity of X-ray absorption, soft X-ray SHG is particularly useful for studying buried interfaces. The atoms of the buried interface can be targeted with minimal absorption of the X-rays as they transmit through the outer layers of the sample, and with minimal SHG generated from interfaces that do not

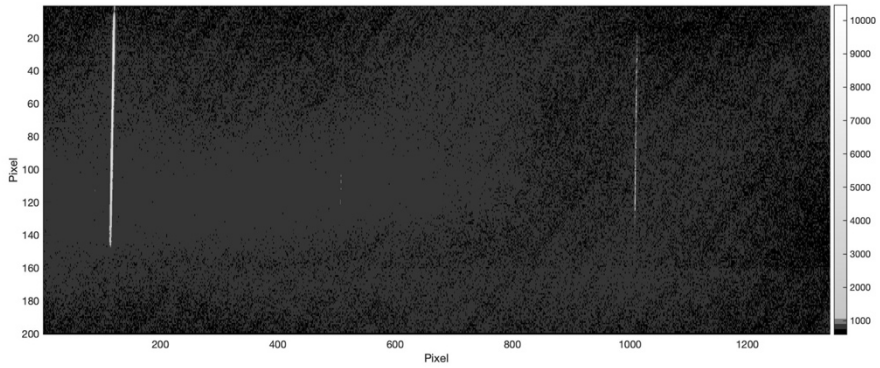

Figure 4.5: Representative CCD Image. CCD image of the fundamental and SHG generated by the B/PN interface. The fundamental was at 188.2 eV and is seen on the CCD at pixels 110 to 125. The SHG is seen at pixels 995 to 1020 which corresponds to a photon energy of 386.4 eV. Baseline correction for the fundamental was performed using adjacent pixels (125 to 140) and the same was done for the SHG using pixels 1020 to 1045.

contain the target element. Another advantage of soft X-ray SHG is that it does not require the very smooth surfaces needed for grazing incidence techniques, and so it is more generally applicable.

X-ray nonlinear spectroscopy has been limited by the availability of sources with sufficient coherence and flux, but the recent advent of X-ray free electron lasers (FELs) that generate femtosecond pulses with high peak powers and coherence makes these experiments more widely accessible. [23–25]. This has led to hard X-ray SHG and SFG studies that demonstrated the bulk-sensitive technique [21,22], as well as soft X-ray SHG studies showing that the technique is interface-sensitive, and that the signal is enhanced when resonant with real transitions in the material [10,11].

Here, we demonstrate the sensitivity of soft X-ray SHG to the buried interface of a boron film with a coating of Parylene-N, a prototypical polymer insulator-semiconductor interface. This buried interface cannot be studied with visible SHG because visible light will be strongly absorbed by the materials. Additionally, the layers are too thick for scanning probe techniques and X-ray photoelectron spectroscopy, and insufficiently smooth for grazing incidence techniques. In this experiment, we compare the soft X-ray SHG spectra of the boron/vacuum (B/V) and boron/Parylene-N (B/PN) interfaces (Fig. 4.4), providing the first demonstration of this technique as a probe of a buried interface. TEY XAS measurements, typically considered surface-sensitive due to the limits of the electron escape depth [17,26], are largely indistinguishable for the two interfaces, but there is a clear difference in their SHG spectra. Finally, we report a detailed first principles calculation of the soft X-ray SHG spectra for both interfaces to interpret the signals, showing that this technique is sensitive to weakening of boron-boron bonds at the B/PN interfacial region.

4.2.1. Experimental Details

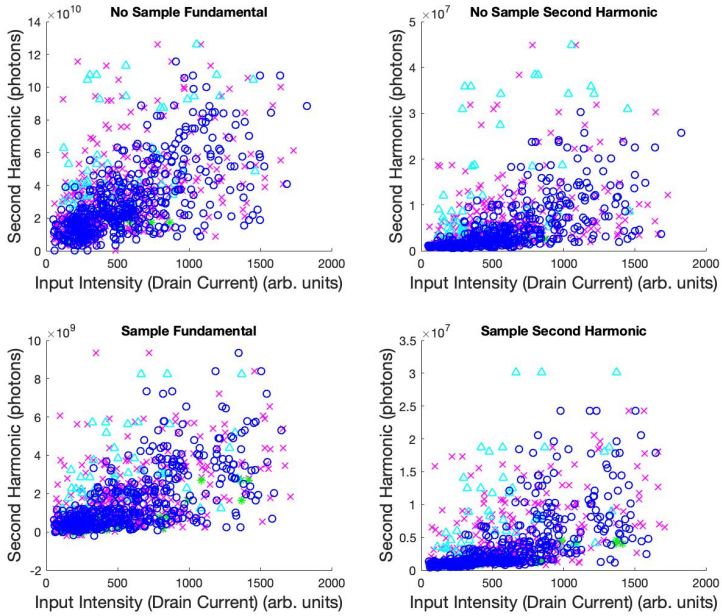

Figure 4.6: Plot of all laser shots vs. input drain current. Data taken at an input photon energy of 191 eV is shown in this plot. The total fundamental signal intensity (a) and total SHG signal intensity (b) with no sample are shown along with the fundamental (c) and SHG (d) signal intensities with the B/PN sample in place. Points were filtered and removed based on the pulse spectrum (x), fundamental signal FWHM (*), and bin outliers (Δ). Only the remaining points (o) are used in further calculations.

At the EIS-TIMEX beamline at FERMI [27], the SHG signal from the sample was detected using the same apparatus as in our previous work [10]. In order to access input photon energies from 184 to 195 eV, the 13th harmonic of FEL-1 and the 3rd harmonic of FEL-2 were used. The energy was tuned within this range by using the OPA to adjust the seed laser photon energies. Photon energies from 195 to 200 eV were accessed using the 10th harmonic of FEL-1 and the 4th harmonic of FEL-2.These fundamental input energies were just below, at, and just above the boron K-edge [28]. In order to examine the SH intensity as a function of input intensity, the input intensity was varied using different metallic filters before the sample (100 nm of Zr, 100 nm of Pd, and 200 nm of Pd). The input intensity (I_0) of the FEL was determined from a photodiode upstream of the sample. An iris was also used upstream of the sample to minimize the off-axis light from the FEL incident on the sample and detector. At the sample, the FEL was focused to a ~10 μm diameter spot. After the sample, the fundamental intensity was attenuated using 200 nm of aluminum before passing through a slit. Both the fundamental and SHG signal were detected simultaneously using a soft X-ray spectrometer (2400 groove/mm spherical grating) and CCD (Princeton Instruments PIXIS-XO 400B) [29]. The samples comprised an unsupported 200 nm boron film and a 200 nm boron film with a 100 nm Parylene-N support layer, purchased from Lebow Corporation.

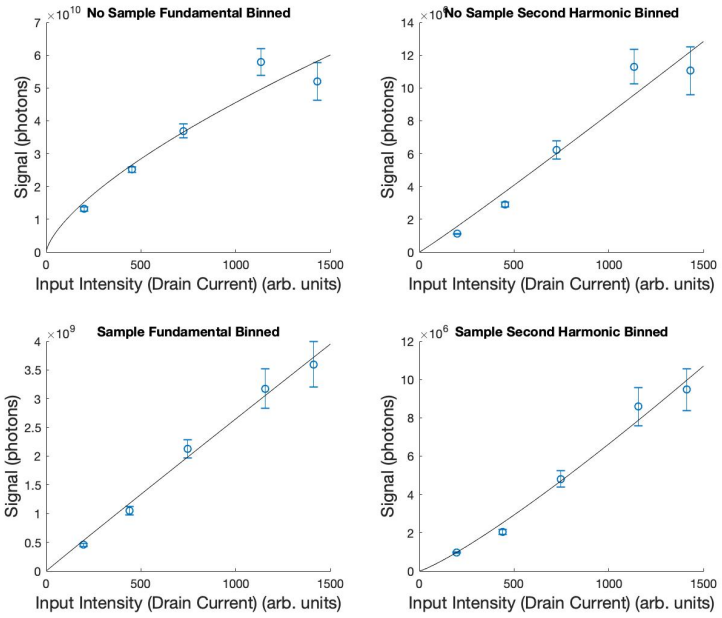

Figure 4.7: Binned and filtered signal vs. input drain current. The binned and filtered signals for the fundamental (a) and SHG (b) without a sample, and the fundamental (c) and SHG (d) with the B/PN sample are shown for an input energy of 191 eV.

The filter transmissions were calculated using the fundamental signal detected by the CCD when there was no sample in place. The exact photon energies of the FEL were also calculated using the position of the fundamental signal on the CCD. A representative CCD image is shown in Figure 4.5 for the data taken with an input energy of 188.2 eV and the boron/Parylene-N (B/PN) sample. The total intensity of each signal is determined by summing the intensities of all the

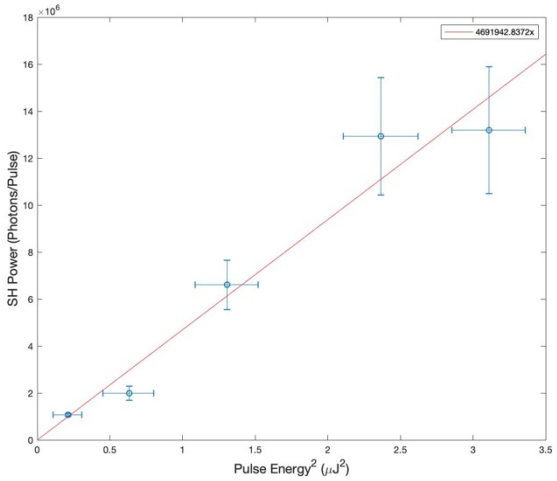

Figure 4.8: SHG generated by the sample vs. pulse energy squared. The SHG signal generated by the B/PN sample with an input photon energy of 191 eV is shown. The slope of the linear fit (4.6 x 10^6) is proportional to $|\chi^{(2)}|$.

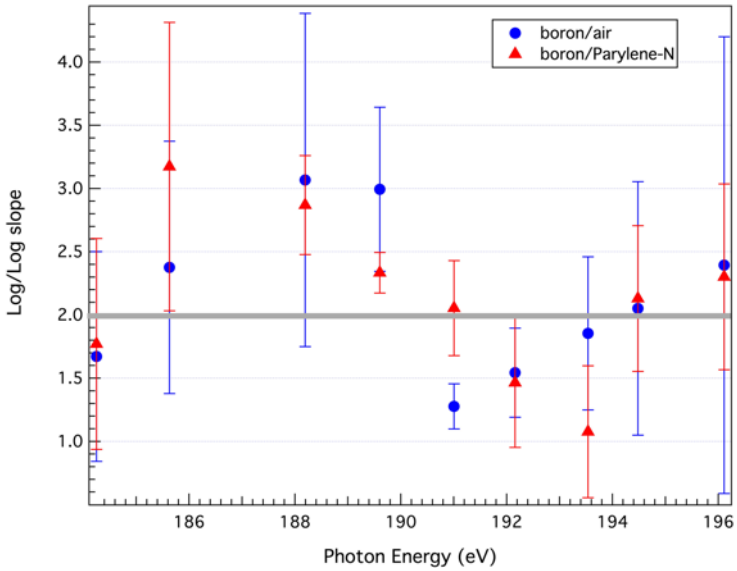

Figure 4.9: Log-log slopes for all datasets. The log-log slopes are shown with their standard errors for all wavelengths and both samples, verifying that the signal we are seeing is in fact SHG. For a quadratic function, the log-log slope will be 2.

pixels in the region of interest (ROI). Baseline corrections were done by subtracting the intensity of a ROI adjacent to that of the signal from the signal intensity.

In our previous X-ray SHG work, it was found that the SHG signal was very sensitive to the quality of the FEL laser pulse [10]. Therefore, each FEL shot was filtered by the spectrum of the pulse collected before the sample (Fig. 4.6) [31]. If the spectrum was not sufficiently gaussian and contains side peaks that are more than 20% of the height of the main peak, the laser pulse is excluded from further analysis. Similarly, the distribution of FWHMs of the funda [113]mental signal on the CCD is examined and any outliers of the FWHM box plot are filtered. The data is then binned (Fig. 4.7), with bins of 400 μJ used at lower intensities and bins of 300 μJ used at higher intensities. The distribution of signals within each bin is also calculated and outliers that lie beyond the outer fence of the box plot are filtered. The binned data is fit with a power series and the fit of the fundamental data taken with no sample is used to calibrate the input pulse energy axis. The SHG signal from the FEL (i.e., the SHG signal seen in the no sample data sets) is subtracted from the SHG signal of the sample. Standard transmission values for aluminum, boron, and Parylene-N were used to account for the effects of the aluminum filter after the sample, and transmission through the sample itself [30]. The signal is also corrected for the detector efficiency.

The intensity of the generated SHG response is given by the relation

$$I_{SHG} \propto \left|\chi^{(2)}\right|^2 I_0^2$$

where $\left|\chi^{(2)}\right|$ is the nonlinear susceptibility of the interface. The SHG intensity was plotted against I_0^2 for each input energy and fit with a linear regression (Fig. 4.7). As can be seen in the

equation the resulting slope is proportional to $|\chi^{(2)}|$. The SHG intensity was plotted against I_0^2 for each input energy and fit with a linear regression. The resulting slope is proportional to the nonlinear susceptibility, $|\chi^{(2)}|$. Finally, this slope was plotted as a function of wavelength to generate the SHG spectrum of the material surface. To confirm that the dependence is truly quadratic, as should be the case for SHG, a plot of log(signal) vs. log(input energy) can be fit to a line. A quadratic function will result in a log-log plot with a slope of 2. As can be seen in Figure 4.8, the datasets all have slopes close to 2 and so we can say we are indeed seeing SHG. TEY X-ray absorption spectra of the two materials were taken at Beamline 8-2 at SSRL [32,33].

Theoretical calculations of the SHG response of the system were performed from first principles

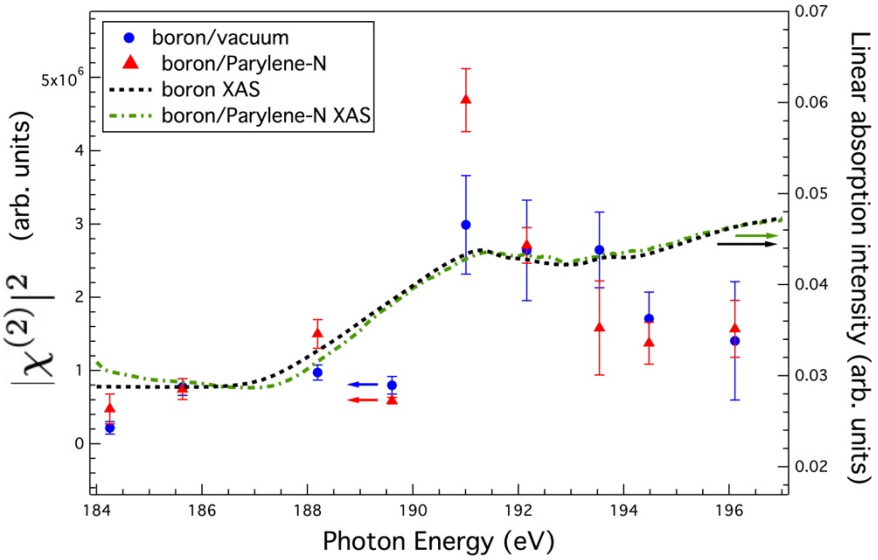

Figure 4.10: Second harmonic generation spectra of the boron/vacuum and boron/Parylene-N interfaces. The SHG spectrum of the B/V (blue circle) and B/PN (red triangle) interfaces are shown along with the linear X-ray absorption of the boron film (black dash) and boron Parylene-N multilayer film (green dash-dot). $|\chi^{(2)}|$ was determined from the linear regression slope of the SHG signal vs. I_0^2. $|\chi^{(2)}|$ is significantly higher at the boron K-edge for B/PN than for B/V.

via perturbation theory within density functional theory [10,34,35]. The B/V SHG calculation was performed using two layers of boron icosahedral unit cells. The B/PN calculation was performed using a single xylene monomer on top of a boron unit cell (Fig. 4.4). The xylene orientation shown in Figure 4.11 was chosen due to constraints on the size of the unit cell. A larger unit cell is required to have the xylene ring parallel to the interface, and this is one avenue that we will explore in the future. The geometry of the monomer was initially optimized using UFF [36]. Next, the structure was further optimized using cp2k [37]. A larger simulation cell could not be used for the B/PN simulations due to the complexity of such a system involving multiple atoms and requiring fine k-point grids. However, previous simulations have shown that the majority of the SHG signal is generated in the first layer, and so these simulations are still useful as a qualitative comparison [10]. The B/V simulation was performed with two layers of boron, to enable accurate comparison with the B/PN simulations. No significant difference is seen between the SHG signal from two layers and three layers of boron.

4.2.2. Discussion

The measured SHG spectra of the B/V and B/PN interfaces are shown in Figure 4.9. Resonance effects can be seen in both spectra, as the SHG intensity increases when the fundamental energy is at or above the boron K-edge. There is no apparent shift in the photon energy that is resonant with the boron K-edge transition. The SHG intensity at the boron K-edge is significantly higher for B/PN than for B/V, while below and above the edge, the two are within error of each other. In contrast, there are no major differences in the linear, TEY X-ray absorption spectra of the two materials (Fig. 4.10). The TEY spectra are essentially identical, indicating that this technique is not sensitive enough to the interface to capture the differences seen in the present SHG spectra. It should be noted that while it is possible for some SHG to be generated at the back B/V interface, this contribution will be smaller than that of the front interface due to absorption of the fundamental through the boron layer. Additionally, the back B/V interface is the same for both samples, and so will not affect any qualitative comparisons between the two interfaces.

Simulations reveal a shift in the boron K-edge at the B/PN interface (Fig. 4.11). Compared to the B/V interface, there is a redshift of about 2.5 eV, and an increase in intensity just above the band edge. Density of states calculations indicate that the core energy levels lie at higher energy in the B/PN system when compared to B/V, as interactions with the Parylene-N have weakened the

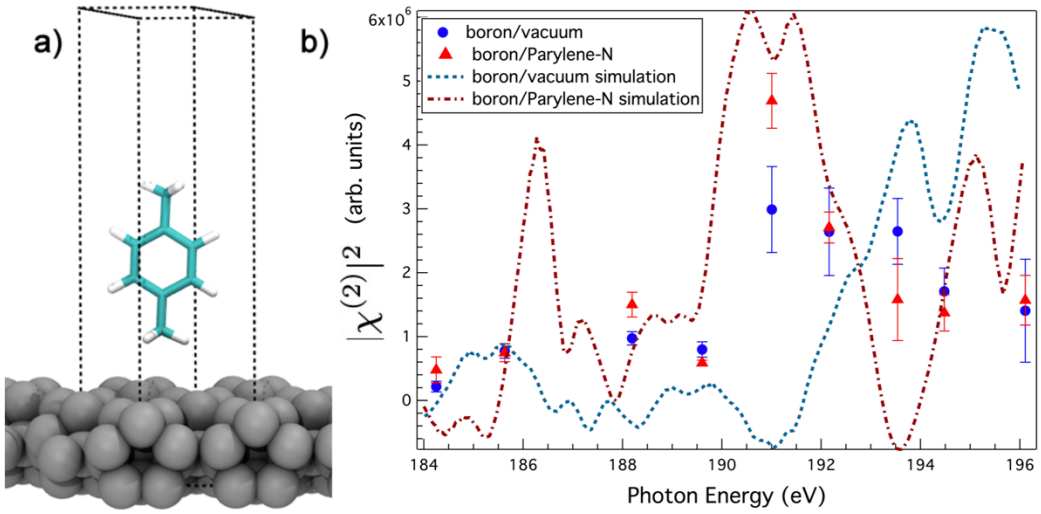

Figure 4.11: Theoretical simulations of $|\chi^{(2)}|$ for the two studied interfaces. The unit cell used for the B/PN calculation is shown in (a). The calculated $|\chi^{(2)}|$ is shown in (b) as a function of input energy for the B/V (blue, dashed) and B/PN (red, dashed) interfaces. The plot also includes the experimental SHG slopes for comparison. In the simulations, there is a shift of the boron K-edge to lower to energy, which is consistent with the increased SHG slope at 191 eV seen in the experiments. The pre-peak at 186 eV is likely due to new transitions being allowed due to symmetry breaking by the Parylene-N layer.

bonds within the boron. Thus, there is a redshift of the K-edge. There is also a pre-edge peak at 186 eV in the B/PN simulated SH spectrum. This peak is likely due to symmetry breaking that allows for excitation of the core electrons into new states. The energy axis of these simulations was calibrated using the same energy shift needed for the linear absorption simulations to align with our experiment. The electrostatic potential due to the presence of a dipole in vertical

direction was also calculated, but the result shows that the effect is negligible, and so a dipole correction is not required. Results for a coarser-grid simulation of two layers of boron and one layer of Parylene-N were very similar to that for one layer of boron and one layer of Parylene-N. Given resonant conditions, the SHG signal in this energy range is almost entirely due to the boron layer, such that adding multiple Parylene-N layers to the simulation will cause negligible changes in the calculated spectrum. The increase in SH intensity found in the experiments is consistent with the redshift. However, because the experiments have low energy resolution, it is not obvious that there is a shift in the spectrum. Further SHG studies at the boron K-edge would clarify this result.

We obtained linear XAS and SHG spectra of the B/V interface and the B/PN buried interface. While there is no observable difference between the two interfaces in the XAS spectra, the spectrum of B/PN shows a distinct increase in SHG intensity at the boron K-edge. This is consistent with theoretical simulations that show a shift of the boron K-edge to lower energy at the B/PN interface due to weakening of interfacial boron-boron bonds. These experiments show that soft X-ray SHG is sensitive to changes in the electronic structure at the interface, which is difficult to probe with other methods. Having established the efficacy of this technique for studying buried interfaces, soft X-ray SHG can be used to probe interfaces in electronics that are difficult to study with other methods, but critical to system functions. The technique has great potential for future studies of buried interfaces in electrochemical cells and catalysts.

4.2.3. References

[1] H. Hong, R. D. Aburano, D.-S. Lin, H. Chen, T.-C. Chiang, P. Zschack, and E. D. Specht, Phys. Rev. Lett. **68**, 507 (1992).

[2] E. Gann, A. Watson, J. R. Tumbleston, J. Cochran, H. Yan, C. Wang, J. Seok, M. Chabinyc, and H. Ade, Phys. Rev. B **90**, 245421 (2014).

[3] C. T. Williams and D. A. Beattie, Surface Science **500**, 545 (2002).

[4] A. J. Hopkins, C. L. McFearin, and G. L. Richmond, Current Opinion in Solid State and Materials Science **9**, 19 (2005).

[5] N. Shibata, S. D. Findlay, S. Azuma, T. Mizoguchi, T. Yamamoto, and Y. Ikuhara, Nature Materials **8**, 654 (2009).

[6] P. Han, A. R. Kurland, A. N. Giordano, S. U. Nanayakkara, M. M. Blake, C. M. Pochas, and P. S. Weiss, ACS Nano **3**, 3115 (2009).

[7] J. C. Conboy, J. L. Daschbach, and G. L. Richmond, Appl. Phys. A **59**, 623 (1994).

[8] J. C. Conboy and G. L. Richmond, J. Phys. Chem. B **101**, 983 (1997).

[9] A. M. Jubb, D. Verreault, R. Posner, L. J. Criscenti, L. E. Katz, and H. C. Allen, Journal of Colloid and Interface Science **400**, 140 (2013).

[10] R. K. Lam, S. L. Raj, T. A. Pascal, C. D. Pemmaraju, L. Foglia, A. Simoncig, N. Fabris, P. Miotti, C. J. Hull, A. M. Rizzuto, J. W. Smith, R. Mincigrucci, C. Masciovecchio, A. Gessini, E. Allaria, G. De Ninno, B. Diviacco, E. Roussel, S. Spampinati, G. Penco, S. Di Mitri, M. Trovò, M. Danailov, S. T. Christensen, D. Sokaras, T.-C. Weng, M. Coreno, L. Poletto, W. S. Drisdell, D. Prendergast, L. Giannessi, E. Principi, D. Nordlund, R. J. Saykally, and C. P. Schwartz, Phys. Rev. Lett. **120**, 023901 (2018).

[11] Sh. Yamamoto, T. Omi, H. Akai, Y. Kubota, Y. Takahashi, Y. Suzuki, Y. Hirata, K. Yamamoto, R. Yukawa, K. Horiba, H. Yumoto, T. Koyama, H. Ohashi, S. Owada, K. Tono, M. Yabashi, E. Shigemasa, S. Yamamoto, M. Kotsugi, H. Wadati, H. Kumigashira, T. Arima, S. Shin, and I. Matsuda, Physical Review Letters **120**, (2018).
[12] J. Stöhr, *NEXAFS Spectroscopy* (Springer Berlin Heidelberg, Berlin, Heidelberg, 1992).
[13] A. J. Achkar, T. Z. Regier, H. Wadati, Y.-J. Kim, H. Zhang, and D. G. Hawthorn, Phys. Rev. B **83**, 081106 (2011).
[14] N. Ottosson, M. Faubel, S. E. Bradforth, P. Jungwirth, and B. Winter, Journal of Electron Spectroscopy and Related Phenomena **177**, 60 (2010).
[15] M. P. Seah and W. A. Dench, Surface and Interface Analysis **1**, 2 (1979).
[16] S. Hüfner, Photoelectron Spectroscopy: Principles and Applications (Springer, Berlin; New York, 1996).
[17] B. H. Frazer, B. Gilbert, B. R. Sonderegger, and G. De Stasio, Surface Science **537**, 161 (2003).
[18] Y. R. Shen, Annu. Rev. Phys. Chem. **40**, 327 (1989).
[19] K. B. Eisenthal, Annu. Rev. Phys. Chem. **43**, 627 (1992).
[20] A. G. Lambert, P. B. Davies, and D. J. Neivandt, Applied Spectroscopy Reviews **40**, 103 (2005).
[21] T. E. Glover, D. M. Fritz, M. Cammarata, T. K. Allison, S. Coh, J. M. Feldkamp, H. Lemke, D. Zhu, Y. Feng, R. N. Coffee, M. Fuchs, S. Ghimire, J. Chen, S. Shwartz, D. A. Reis, S. E. Harris, and J. B. Hastings, Nature **488**, 603 (2012).
[22] S. Shwartz, M. Fuchs, J. B. Hastings, Y. Inubushi, T. Ishikawa, T. Katayama, D. A. Reis, T. Sato, K. Tono, M. Yabashi, S. Yudovich, and S. E. Harris, Phys. Rev. Lett. **112**, 163901 (2014).
[23] E. Allaria, R. Appio, L. Badano, W. A. Barletta, S. Bassanese, S. G. Biedron, A. Borga, E. Busetto, D. Castronovo, P. Cinquegrana, S. Cleva, D. Cocco, M. Cornacchia, P. Craievich, I. Cudin, G. D'Auria, M. Dal Forno, M. B. Danailov, R. De Monte, G. De Ninno, P. Delgiusto, A. Demidovich, S. Di Mitri, B. Diviacco, A. Fabris, R. Fabris, W. Fawley, M. Ferianis, E. Ferrari, S. Ferry, L. Froehlich, P. Furlan, G. Gaio, F. Gelmetti, L. Giannessi, M. Giannini, R. Gobessi, R. Ivanov, E. Karantzoulis, M. Lonza, A. Lutman, B. Mahieu, M. Milloch, S. V. Milton, M. Musardo, I. Nikolov, S. Noe, F. Parmigiani, G. Penco, M. Petronio, L. Pivetta, M. Predonzani, F. Rossi, L. Rumiz, A. Salom, C. Scafuri, C. Serpico, P. Sigalotti, S. Spampinati, C. Spezzani, M. Svandrlik, C. Svetina, S. Tazzari, M. Trovo, R. Umer, A. Vascotto, M. Veronese, R. Visintini, M. Zaccaria, D. Zangrando, and M. Zangrando, Nature Photonics **6**, 699 (2012).
[24] E. Allaria, D. Castronovo, P. Cinquegrana, P. Craievich, M. Dal Forno, M. B. Danailov, G. D'Auria, A. Demidovich, G. De Ninno, S. Di Mitri, B. Diviacco, W. M. Fawley, M. Ferianis, E. Ferrari, L. Froehlich, G. Gaio, D. Gauthier, L. Giannessi, R. Ivanov, B. Mahieu, N. Mahne, I. Nikolov, F. Parmigiani, G. Penco, L. Raimondi, C. Scafuri, C. Serpico, P. Sigalotti, S. Spampinati, C. Spezzani, M. Svandrlik, C. Svetina, M. Trovo, M. Veronese, D. Zangrando, and M. Zangrando, Nature Photonics **7**, 913 (2013).
[25] N. Rohringer, D. Ryan, R. A. London, M. Purvis, F. Albert, J. Dunn, J. D. Bozek, C. Bostedt, A. Graf, R. Hill, S. P. Hau-Riege, and J. J. Rocca, Nature **481**, 488 (2012).
[26] M. Abbate, J. B. Goedkoop, F. M. F. de Groot, M. Grioni, J. C. Fuggle, S. Hofmann, H. Petersen, and M. Sacchi, Surface and Interface Analysis **18**, 65 (1992).

[27] C. Masciovecchio, A. Battistoni, E. Giangrisostomi, F. Bencivenga, E. Principi, R. Mincigrucci, R. Cucini, A. Gessini, F. D'Amico, R. Borghes, M. Prica, V. Chenda, M. Scarcia, G. Gaio, G. Kurdi, A. Demidovich, M. B. Danailov, A. Di Cicco, A. Filipponi, R. Gunnella, K. Hatada, N. Mahne, L. Raimondi, C. Svetina, R. Godnig, A. Abrami, and M. Zangrando, Journal of Synchrotron Radiation **22**, 553 (2015).
[28] A. Majhi, M. Nayak, P. C. Pradhan, E. O. Filatova, A. Sokolov, and F. Schäfers, Sci Rep **8**, 15724 (2018).
[29] L. Poletto, F. Frassetto, P. Miotti, A. Di Cicco, P. Finetti, C. Grazioli, F. Iesari, A. Kivimäki, S. Stagira, and M. Coreno, Review of Scientific Instruments **85**, 103112 (2014).
[30] B. L. Henke, E. M. Gullikson, and J. C. Davis, Atomic Data and Nuclear Data Tables **54**, 181 (1993).
[31] M. Zangrando, D. Cocco, C. Fava, S. Gerusina, R. Gobessi, N. Mahne, E. Mazzucco, L. Raimondi, L. Rumiz, and C. Svetina, J Synchrotron Rad **22**, 565 (2015).
[32] L. J. Terminello, G. D. Waddill, and J. G. Tobin, Nuclear Instruments and Methods in Physics Research Section A: Accelerators, Spectrometers, Detectors and Associated Equipment **319**, 271 (1992).
[33] K. G. Tirsell and V. P. Karpenko, Nuclear Instruments and Methods in Physics Research Section A: Accelerators, Spectrometers, Detectors and Associated Equipment **291**, 511 (1990).
[34] S. Sharma and C. Ambrosch-Draxl, Phys. Scr. **2004**, 128 (2004).
[35] A. Gulans, S. Kontur, C. Meisenbichler, D. Nabok, P. Pavone, Santiago Rigamonti, S. Sagmeister, U. Werner, and C. Draxl, J. Phys.: Condens. Matter **26**, 363202 (2014).
[36] A. K. Rappe, C. J. Casewit, K. S. Colwell, W. A. Goddard, and W. M. Skiff, J. Am. Chem. Soc. **114**, 10024 (1992).
[37] J. Hutter, M. Iannuzzi, F. Schiffmann, and J. VandeVondele, Wiley Interdisciplinary Reviews: Computational Molecular Science **4**, 15 (2014).

Chapter 5: Summary and Future Work

5.1. Summary

The liquid state of carbon is very poorly understood due to the extreme temperatures and pressures required for its formation (above 5,000 K and 10 MPa). However, understanding it will open up new avenues in our fundamental understanding of the carbon phase diagram, as well as answering questions about tetrahedral liquids and possible liquid-liquid phase transitions. Additionally, liquid carbon could be essential for understanding planets and stars with high carbon content as well as the formation of exotic carbon states. The latest *ab initio* theoretical studies suggest that the liquid is made of *sp* bonded chains and is insulating at low pressures. As its density increases, it increases in coordination and eventually develops metallic properties. Experiments on liquid carbon have been limited by difficulties in preparing it, and initial studies of graphite melting were performed using electrical heating. More recently, shock compression has been used to generate liquid and warm dense carbon.

Non-thermal melting is an elegant tool that allows for transient generation of liquid carbon under ambient pressure. Using an ultrafast laser pulse, significant electronic excitation weakens bonds in the solid and causes reorganization into a liquid before thermalization occurs. The liquid is inertially confined to the original solid density and will expand and ablate over many picoseconds. Using non-thermal melting of different carbon substrates, the visible reflectivity of different densities of liquid carbon has been studied. X-ray absorption has also been used to characterize the fraction of σ and π bonds found in the liquid at various densities.

In this dissertation, we have expanded on the initial extreme-UV reflectivity experiments addressing non-thermally melted carbon. This technique, unlike visible reflectivity, is only sensitive to the lattice dynamics and not to the hot electron plasma generated by the melting pulse. The liquid reflectivity was probed over time as it was formed and later ablated. Probe wavelengths from 21 nm to 42 nm were used with both *s* and *p* polarizations. At all the wavelengths studied, the reflectivity decayed with time constants below 10 ps. At longer probe wavelengths, the time constants increase due to contributions from the hot electron plasma. The calculated electronic temperature of the melted carbon is less than the value calculated from a two-temperature model, suggesting that more complex dynamics are required to explain the evolution of the material. The two polarizations were also used to calculate the time evolution of the complex refractive index of the material.

To gain a better understanding of the coordination behavior in the liquid, chirped coherent anti-Stokes Raman spectroscopy (c-CARS) measurements of nonthermally melted liquid carbon were attempted. The c-CARS pump was a chirped picosecond pulse which interacted with a broadband femtosecond CARS probe to generate a high resolution, broadband CARS spectrum. The graphite sample was melted with 800 nm melting pulse at fluences well over the melting threshold. Contrary to expectations, there was no apparent broadening or shifting of the graphite G-peak. Only the intensity of the peak decreases over time. It remains unclear why there was no change in this peak.

Ultrafast soft X-ray second harmonic generation (SHG), was developed in order to provide a new atom-selective approach for studying liquid carbon, unique carbon states, and solid-solid interfaces that are difficult to study with other techniques. We obtained the first soft X-ray SHG signal from graphite films and showed that it was indeed as highly surface specific in the soft X-ray regime as it is in the IR to UV regimes. We then demonstrated the use of this technique for the study of buried interfaces using a boron and Parylene-N multilayer film. Theoretical simulations confirm the interfacial sensitivity of this technique.

5.2. Future Directions

Many interesting questions regarding liquid carbon remain to be answered. Our research group is involved in a number of new experiments to expand our knowledge of this material. Resonant inelastic X-ray scattering experiments have been performed with free electron lasers on non-thermally melted amorphous carbon. These studies show interesting time dynamics that will require both further experiments and theoretical work to be fully explained. Grazing incidence X-ray diffraction experiments on liquid carbon are also ongoing. Building on our soft X-ray SHG work, soft X-ray sum frequency generation spectroscopy can be used to probe the surface of non-thermally melted liquid carbon. This is of particular interest, as the surface could play a key role in the generation of unique metastable carbon materials. Finally, to continue the work in this dissertation, CARS studies of different carbon materials, as well as studies of other non-thermally melted materials, may provide new insight into the results obtained thus far, and thus would aid in advancing our understanding of the coordination and dynamics of liquid carbon.